

GALERKIN NEURAL NETWORK-POD FOR ACOUSTIC AND ELECTROMAGNETIC WAVE PROPAGATION IN PARAMETRIC DOMAINS

PHILIPP WEDER[†], MARIELLA KAST[†], FERNANDO HENRÍQUEZ[†], AND JAN S. HESTHAVEN[†]

ABSTRACT. We investigate reduced-order models for acoustic and electromagnetic wave problems in parametrically defined domains. The parameter-to-solution maps are approximated following the so-called Galerkin POD-NN method, which combines the construction of a reduced basis via proper orthogonal decomposition (POD) with neural networks (NNs). As opposed to the standard reduced basis method, this approach allows for the swift and efficient evaluation of reduced-order solutions for any given parametric input.

As is customary in the analysis of problems in random or parametrically defined domains, we start by transporting the formulation to a reference domain. This yields a parameter-dependent variational problem set on parameter-independent functional spaces. In particular, we consider affine-parametric domain transformations characterized by a high-dimensional, possibly countably infinite, parametric input. To keep the number of evaluations of the high-fidelity solutions manageable, we propose using low-discrepancy sequences to sample the parameter space efficiently. Then, we train an NN to learn the coefficients in the reduced representation. This approach completely decouples the offline and online stages of the reduced basis paradigm.

Numerical results for the three-dimensional Helmholtz and Maxwell equations confirm the method's accuracy up to a certain barrier and show significant gains in online speed-up compared to the traditional Galerkin POD method.

1. INTRODUCTION

Partial differential equations (PDEs) are a ubiquitous approach to physical modeling in engineering and the applied sciences. However, knowledge of the underlying parameters, such as boundary conditions, source terms, or geometry, is often incomplete. Consequentially, parameters are often varied during the search for a specific configuration of the system, e.g., in parameter estimation [55], topology optimization [6], optimal control [54], or uncertainty quantification [51]. As these methods require repeated evaluations of the parameterized PDE problem, one speaks of *many-query problems*.

The standard discretization techniques, such as the finite element, finite difference, or finite volume methods, allow precise approximations of the solutions to parameterized PDEs (pPDEs). Yet, such high-fidelity (HF) approximations are intrinsically linked to a prohibitive computational complexity for many-query or real-time applications. *Reduced-order modeling* (ROM) aims at constructing fast surrogate models to accelerate the computation of the approximate solution to a given pPDE problem while retaining an accuracy comparable to that of HF techniques. One common approach to ROM are *reduced basis* (RB) methods. They are based on an *offline-online paradigm*, where first, a reduced basis is constructed from a number of expensive high-fidelity snapshots (offline step). Then, a fast surrogate model is evaluated in the reduced basis (online step). For a comprehensive review of the RB method for stationary problems with certified error control, we refer to [34, 48, 47, 49].

In this work, we focus on the construction of surrogate models from a reduced basis obtained by the proper orthogonal decomposition (POD). For the Galerkin POD method, the full-order system is projected onto the reduced space, which leads to a reduced system of equations for the RB coefficients. Although effective, this approach does not yield the desired computational

[†]CHAIR OF COMPUTATIONAL MATHEMATICS AND SIMULATION SCIENCE (MCSS), ÉCOLE POLYTECHNIQUE FÉDÉRALE DE LAUSANNE, LAUSANNE, SWITZERLAND.

E-mail addresses: philipp.weder@epfl.ch, mariella.kast@epfl.ch, fernando.henriquez@epfl.ch, jan.hesthaven@epfl.ch.

speed-up in the general case, as the full-order solution still needs to be assembled in the online stage to evaluate the PDE operators. Various intrusive techniques aim at alleviating this issue, for example, by exploiting affine parameter-dependencies [34, Chapter 3.3] or using hyper-reduction [34, Chapter 5] to approximate reduced order terms directly.

In contrast, non-intrusive RB methods only rely on HF snapshots and typically construct a surrogate of the map from parameters to RB coefficients. To obtain the response surface, a data-driven regression problem is formulated on the set of RB coefficients of HF snapshots at evaluated parameter location. Then, a query of the surrogate model allows for the solution evaluation of a new, unseen parameter setting. The response surface has to be able to capture the non-linear structure of the underlying parameter-to-solution map of the PDE problem, which makes neural networks [33] or Gaussian processes [23] suitable choices. In this work, we explore the construction of projection-based reduced-order models for acoustic and electromagnetic scattering, which are modeled by the Helmholtz and time-harmonic Maxwell equations, respectively. For both cases, we consider computational domains with parametrically defined geometries. Such models are of interest in a variety of applications, e.g. metallic meta-materials [4], and the design of thermovoltaic cells [11].

In particular, we are interested in studying affine-parametric domain deformations with a high-dimensional, possibly countable infinite, parametric input, which leads to a computationally challenging, high-dimensional parameter-to-solution map. Numerous techniques exist which are tailored to treat efficiently problems with high-dimensional inputs, such as sparse grid interpolation and quadrature [57, 43, 24], higher-order Quasi-Monte Carlo integration (HoQMC)[16, 17], construction of NN surrogates [50, 32, 44, 31, 1], and model order reduction [9]. As pointed out in [12], a key property to break the so-called *curse of dimensionality* in the parameter space is the holomorphic dependence of the parameter-to-solution map. This property has been established for a variety of problems, including for example subsurface flows [8, 26, 27], time-harmonic electromagnetic wave scattering [37, 2], stationary Stokes and Navier-Stokes equation [14], Helmholtz equation [35, 53, 22], and for boundary integral operators [30, 28, 46, 18, 15, 29].

Contributions. We theoretically and computationally study the performance of the POD-NN applied to the Helmholtz interior impedance problem and the Maxwell lossy cavity with affine-parametric shape deformations previously used in [2]. The parametric holomorphy property, which is crucial for the effectiveness of dimensionality reduction, has previously been established for the Maxwell lossy cavity problem. For the sake of completeness, we provide the corresponding proof for the Helmholtz impedance problem.

To approximate the complex-valued reduced order coefficients, we modify the POD-NN approach in [33] and propose an NN architecture, which models the real and imaginary parts of each reduced coefficient as separate outputs. We show that this does not affect the holomorphy property, indicating that this modified map can also be emulated by NNs. To further facilitate the learning task, we propose a centered POD approach. To justify the effectiveness of the POD-NN approach, we further provide a complete convergence analysis for the reduced basis method for the two model problems.

Finally, we present a comprehensive set of numerical experiments in which we study the effect of parametric domain transformations with different decay structures, wave numbers of the problems, and hyperparameters of the neural network.

Outline. In Section 2 we introduce the notion of pPDEs, together with a thorough description of the Helmholtz impedance and Maxwell lossy cavity problem in parametric domains. Section 3 introduces the projection-based reduced order modeling for pPDEs and some theoretical properties. Next, in Section 4, we discuss the Galerkin POD-NN approach and its adaptation to complex-valued solution spaces in more detail. In Section 5, we demonstrate the efficacy of our proposed approach and provide insights into the relation between problem complexity and approximation error by varying various hyperparameters. Lastly, in Section 6, we draw conclusions about this method and sketch directions of possible future research.

2. PARAMETRIC PDES: HELMHOLTZ AND MAXWELL FORMULATIONS

In this section, we first state the formulation of pPDEs in a generic fashion, which serves as a common ground to explain the reduced basis method applied to both PDE model problems. Then, we discuss the weak formulations, well-posedness, and discretizations in more detail for the Helmholtz impedance and Maxwell lossy cavity problems.

Following previous works on the subject, we introduce the Galerkin POD for pPDEs, where we put particular emphasis on parametrically defined domains.

2.1. Parametric PDEs. Throughout, let $\mathbf{U} := [-1, 1]^{\mathbb{N}}$ be the parameter space. Let V be a *complex* Hilbert space endowed with the scalar product $(\cdot, \cdot)_V$ and the induced norm $\|\cdot\|_V = \sqrt{(\cdot, \cdot)_V}$. We denote by V' the anti-dual space of V , i.e. the set of all anti-linear functionals acting on V . Then, the differential (strong) form of a pPDE can be expressed as follows: For each $\mathbf{y} \in \mathbf{U}$ we seek $u(\mathbf{y}) \in V$ such that

$$\mathbf{G}(u(\mathbf{y}); \mathbf{y}) = 0, \quad \text{in } V', \quad (2.1)$$

where, for each $\mathbf{y} \in \mathbf{U}$, $\mathbf{G}(\cdot; \mathbf{y}) : V \rightarrow V'$ is an operator representing the action of the underlying PDE. We express (2.1) in a variational form. To this end, for each $\mathbf{y} \in \mathbf{U}$, we define the parameter dependent sesquilinear form $\mathbf{g}(\cdot, \cdot; \mathbf{y}) : V \times V \rightarrow \mathbb{C}$, as

$$\mathbf{g}(u, v; \mathbf{y}) := \langle \mathbf{G}(u; \mathbf{y}), v \rangle_{V' \times V}, \quad \forall u, v \in V,$$

being $\langle \cdot, \cdot \rangle_{V' \times V}$ the duality pairing. Then, the variational formulation of (2.1) reads: Given $\mathbf{y} \in \mathbf{U}$, find $u(\mathbf{y}) \in V$ such that

$$\mathbf{g}(u(\mathbf{y}), v; \mathbf{y}) = 0, \quad \forall v \in V. \quad (2.2)$$

In Sections 2.4 and 2.5, we consider the particular instance of a linear operator \mathbf{G} .

2.2. The Discrete Full-order Model. Let $V_h \subset V$ be a finite dimensional subspace of V of dimension N_h with underlying discretization parameter $h > 0$.

The Galerkin approximation of the variational problem stated in (2.2) reads as follows: For a given $\mathbf{y} \in \mathbf{U}$, find $u_h(\mathbf{y}) \in V_h$ such that

$$\mathbf{g}(u_h(\mathbf{y}), v_h; \mathbf{y}) = 0, \quad \forall v_h \in V_h. \quad (2.3)$$

Let $\{\varphi_1, \dots, \varphi_{N_h}\}$ be a basis of V_h . Each $v_h \in V_h$ admits the following unique representation

$$v_h = \sum_{m=1}^{N_h} c_m(v_h) \varphi_m,$$

where $c_m : V_h \rightarrow \mathbb{C}$ are linear functionals representing the degrees of freedom of the FE space V_h . Therefore, each $v_h \in V_h$ can be uniquely represented by the sequence $\{c_m(v_h)\}_{m=1}^{N_h}$ according to

$$V_h \ni v_h \iff \mathbf{v}_h := (c_1(v_h), \dots, c_{N_h}(v_h))^{\top} \in \mathbb{C}^{N_h}, \quad (2.4)$$

Problem 2.3 can be cast in the following algebraic form: For each $\mathbf{y} \in \mathbf{U}$, find $\mathbf{u}_h(\mathbf{y}) \in \mathbb{C}^{N_h}$ such that

$$\mathbf{G}_h(\mathbf{u}_h(\mathbf{y}); \mathbf{y}) = \mathbf{0} \in \mathbb{C}^{N_h},$$

where the residual vector $\mathbf{G}_h(\mathbf{u}_h; \mathbf{y})$ is defined as

$$(\mathbf{G}_h(\mathbf{u}_h; \mathbf{y}))_i := \mathbf{g}(u_h(\mathbf{y}), \varphi_i), \quad i = 1, \dots, N_h.$$

The solution vector $\mathbf{u}_h(\mathbf{y})$ is obtained by solving a system of linear equations of size $N_h \times N_h$ for linear problems, while in the non-linear case, iterative methods must be employed.

2.3. Parametric Domain Transformations. As previously pointed out, we focus on problem where the parametric input define shape deformations. We consider the following family of parametric domain transformations with respect to a bounded, Lipschitz domain D_0 referred to as the reference domain: For each $\mathbf{y} \in U$, we define $\mathbf{T}(\cdot, \mathbf{y}) : D_0 \rightarrow \mathbb{R}^3$ as

$$\mathbf{T}(\widehat{\mathbf{x}}; \mathbf{y}) := \mathbf{T}_0(\widehat{\mathbf{x}}) + \sum_{j \geq 1} y_j \mathbf{T}_j(\widehat{\mathbf{x}}), \quad \widehat{\mathbf{x}} \in D_0, \quad \mathbf{y} = \{y_j\}_{j \geq 1} \in U,$$

where $\mathbf{T}_j : D_0 \rightarrow \mathbb{R}^3$, $j \in \mathbb{N}_0$. In principle, we allow for possible countable infinite parametric inputs. However, in the practical computational implementation we consider a truncation in the parametric dimension.

In the following, we work under the assumptions stated below.

Assumption 2.1. For $j \in \mathbb{N}$, set $b_j = \|\mathbf{T}_j\|_{W^{1,\infty}(D_0; \mathbb{R}^3)}$.

(i) For each $\mathbf{y} \in U$ the domain transformation $\mathbf{T}(\cdot; \mathbf{y})$ is bijective and bi-Lipschitz, and

$$D(\mathbf{y}) := \{\mathbf{x} \in \mathbb{R}^3 : \mathbf{x} = \mathbf{T}(\widehat{\mathbf{x}}; \mathbf{y}), \widehat{\mathbf{x}} \in D_0\} \quad (2.6)$$

defines a bounded, Lipschitz domain in \mathbb{R}^3 .

(ii) There exists $p \in (0, 1)$ such that $\mathbf{b} = \{b_j\}_{j \in \mathbb{N}} \in \ell^p(\mathbb{N})$.

As in [2], we consider the following setting for the numerical experiments to be presented ahead in Section 5: $D_0 := (-1, 1)^3$, $\mathbf{T}_0(\widehat{\mathbf{x}}) = \widehat{\mathbf{x}}$ together with

$$\mathbf{T}_j(\mathbf{x}) := \mu_j \begin{pmatrix} 0 \\ 0 \\ \sin(\pi j \hat{x}_1) \end{pmatrix}, \quad \mathbf{x} = (\hat{x}_1, \hat{x}_2, \hat{x}_3)^\top \in D_0,$$

i.e. we consider a sinusoidal deformation of the cube in the third coordinate. In addition, we use the following two choices for μ_j .

- **Algebraic Decay.** We assume that $\mu_j(r, \theta) = \theta j^{-(r+1)}$ for $\theta > 0$ and $r > 1$.
- **Matérn-Like Covariance Decay.** We consider the following sequence mimicking the decay of the eigenvalues of the Matérn-Like Covariance operator, see [56] (Chapter 4.2.1) for details, i.e. we set

$$\mu_j(a, \nu, \theta) = \theta \frac{a^\nu}{(a + \pi^2 j^2)^{\nu+0.5}} \frac{\Gamma(\nu + 0.5)}{\Gamma(\nu)}, \quad a = \frac{2\nu}{l^2},$$

where l corresponds to the length scale, ν models the roughness of the perturbation and Γ is the Gamma function. In particular, choosing smaller length scales l leads to reduced importance decay along the first parametric dimensions, which in turns leads to a richer structure of perturbations compared to the algebraic decay. This is visualized ahead in the numerical results section.

Remark 2.2. Observe that for the first case, i.e. the algebraic decay, one has $\{\mu_j(r, \theta)\}_{j \in \mathbb{N}} \in \ell^p(\mathbb{N})$ for $\frac{1}{r} < p < 1$, and in the second case $\{\mu_j(a, \nu, \theta)\}_{j \in \mathbb{N}} \in \ell^p(\mathbb{N})$ for any $\frac{1}{2\nu} < p < 1$.

2.4. The Helmholtz Impedance Problem in Parametric Domains. Herein, we consider the Helmholtz problem equipped with impedance boundary conditions on a parametrically defined, bounded Lipschitz domain $D(\mathbf{y})$, $\mathbf{y} \in U$, with boundary $\Gamma(\mathbf{y}) := \partial D(\mathbf{y})$. Here, $D(\mathbf{y})$ is as in (2.6), i.e. for each $\mathbf{y} \in U$ the image through the affine-parametric domain transformation of the reference domain D_0 .

Let $f \in L^2(D(\mathbf{y}))$, $g \in L^2(\Gamma(\mathbf{y}))$ and $\kappa > 0$ be given. For each $\mathbf{y} \in U$, we consider the problem of finding $u : D(\mathbf{y}) \rightarrow \mathbb{C}$ such that

$$-\Delta u(\mathbf{y}) - \kappa^2 u(\mathbf{y}) = f \quad \text{in } D(\mathbf{y}) \quad \text{and} \quad \frac{\partial u}{\partial \nu_{\Gamma(\mathbf{y})}} - \nu \kappa \gamma_{\Gamma(\mathbf{y})} u(\mathbf{y}) = g \quad \text{on } \Gamma(\mathbf{y}), \quad (2.7)$$

where

$$\frac{\partial u}{\partial \nu_{\Gamma(\mathbf{y})}} : H^1(D(\mathbf{y}), \Delta) \rightarrow H^{-\frac{1}{2}}(\Gamma(\mathbf{y})) \quad \text{and} \quad \gamma_{\Gamma(\mathbf{y})} : H^1(D(\mathbf{y})) \rightarrow H^{\frac{1}{2}}(\Gamma(\mathbf{y})) \quad (2.8)$$

denote the Neumann and Dirichlet trace operators. In (2.8), we have that $H^1(D(\mathbf{y}), \Delta) := \{u \in H^1(D(\mathbf{y})) : \Delta u \in L^2(D(\mathbf{y}))\}$, and $\boldsymbol{\nu}(\mathbf{y})$ signifies the outward-pointing normal vector to $\Gamma(\mathbf{y})$. The interior impedance Helmholtz problem admits the following variational formulation.

Problem 2.3 (Helmholtz Impedance Problem in $D(\mathbf{y})$). *Let $f \in L^2(D(\mathbf{y}))$, $g \in L^2(\Gamma(\mathbf{y}))$ for each $\mathbf{y} \in U$. For each $\mathbf{y} \in U$ we seek $u(\mathbf{y}) \in H^1(D(\mathbf{y}))$ such that*

$$\mathbf{a}(u(\mathbf{y}), v; \mathbf{y}) = \ell(v; \mathbf{y}), \quad \forall v \in H^1(D(\mathbf{y})),$$

where the parameter-dependent sesquilinear form $\mathbf{a}(\cdot, \cdot; \mathbf{y}) : H^1(D(\mathbf{y})) \times H^1(D(\mathbf{y})) \rightarrow \mathbb{C}$ is defined for each $\mathbf{y} \in U$ as

$$\mathbf{a}(u, v; \mathbf{y}) := \int_{D(\mathbf{y})} (\nabla u \cdot \nabla \bar{v} - \kappa^2 u \bar{v}) \, d\mathbf{x} - \kappa \int_{\Gamma(\mathbf{y})} \gamma_{\Gamma(\mathbf{y})} u \gamma_{\Gamma(\mathbf{y})} \bar{v} \, ds, \quad \forall u, v \in H^1(D(\mathbf{y})) \quad (2.9)$$

and the parameter-dependent anti-linear form $\ell(\cdot; \mathbf{y}) : H^1(D(\mathbf{y})) \rightarrow \mathbb{C}$ is defined for each $\mathbf{y} \in U$ as

$$\ell(v; \mathbf{y}) := \int_{D(\mathbf{y})} f \bar{v} \, d\mathbf{x} + \int_{\Gamma(\mathbf{y})} g \gamma_{\Gamma(\mathbf{y})} \bar{v} \, ds_{\mathbf{x}}, \quad \forall v \in H^1(D(\mathbf{y})). \quad (2.10)$$

By invoking the Banach-Nečas-Babuška theorem, Gårding's inequality, and the injectivity of the sesquilinear form $\mathbf{a}(\cdot, \cdot; \mathbf{y}) : H^1(D(\mathbf{y})) \times H^1(D(\mathbf{y})) \rightarrow \mathbb{C}$, one may establish well-posedness of Problem 2.3 (cf. [21, Theorem 35.5]), pointwise for each $\mathbf{y} \in U$.

2.4.1. Helmholtz problem in the reference domain. To recast the integrals in (2.9) and (2.10) in terms of D_0 , we recall the following formulas for domain and boundary transformations, which can be found in [5]. Denote by $d\mathbf{T}(\mathbf{y})$ the Jacobian matrix of the transformation $\mathbf{T}(\mathbf{y})$ and by $J(\mathbf{y})$ its Jacobian determinant. For each $\mathbf{y} \in U$ we define $\Phi(\mathbf{y}) : H^1(D(\mathbf{y})) \rightarrow H^1(D_0)$ as $(\Phi(\mathbf{y})v)(\hat{\mathbf{x}}) = v(\mathbf{T}(\hat{\mathbf{x}}; \mathbf{y}))$, $\hat{\mathbf{x}} \in D_0$, which is usually referred to as the *plain pullback* operator. One has that for each $\mathbf{y} \in U$, $\Phi(\mathbf{y})$ is a bounded linear operator with a bounded inverse, see e.g. [14, Section 3] and [26, Lemma 1].

Furthermore, for each $\mathbf{y} \in U$ we define the surface Jacobian on the boundary $\Gamma(\mathbf{y})$ as

$$J_S(\mathbf{y}) = J(\mathbf{y}) \left\| d\mathbf{T}^{-\top}(\mathbf{y}) \hat{\boldsymbol{\nu}}(\mathbf{y}) \right\| \in L^\infty(D_0)$$

where $\hat{\boldsymbol{\nu}}(\mathbf{y}) := \Phi(\mathbf{y}) \boldsymbol{\nu}_{\Gamma(\mathbf{y})} \in L^\infty(\Gamma_0; \mathbb{R}^3)$. For $\hat{v} \in H^1(D_0)$ we set $v := \Phi^{-1}(\mathbf{y}) \hat{v}$. Then, we have

$$\nabla v = d\mathbf{T}^{-\top} \widehat{\nabla} \hat{v} \circ \mathbf{T}^{-1}, \quad \int_{D(\mathbf{y})} v \, d\mathbf{x} = \int_{D_0} \hat{v} J(\mathbf{y}) \, d\hat{\mathbf{x}}, \quad \text{and} \quad \int_{\Gamma(\mathbf{y})} v \, ds = \int_{\Gamma_0} \hat{v} J_S(\mathbf{y}) \, d\hat{\mathbf{s}}_{\hat{\mathbf{x}}},$$

where the latter identity is also called *Nanson's formula*, and $\widehat{\nabla}$ denotes the gradient operator in the reference domain. This allows us to state the variational formulation for the Helmholtz equation in the reference domain.

Problem 2.4 (Helmholtz Impedance Problem in the Reference Domain). *For each $\mathbf{y} \in U$, we seek $\hat{u}(\mathbf{y}) \in H^1(D_0)$ such that*

$$\hat{\mathbf{a}}(\hat{u}(\mathbf{y}), \hat{v}; \mathbf{y}) = \hat{\ell}(\hat{v}; \mathbf{y}), \quad \forall \hat{v} \in H^1(D_0),$$

where for each $\mathbf{y} \in U$ the sesquilinear form $\hat{\mathbf{a}}(\cdot, \cdot; \mathbf{y}) : H^1(D_0) \times H^1(D_0) \rightarrow \mathbb{C}$ is defined as

$$\begin{aligned} \hat{\mathbf{a}}(\hat{v}, \hat{w}; \mathbf{y}) := & \int_{D_0} \left(d\mathbf{T}^{-\top}(\mathbf{y}) \widehat{\nabla} \hat{v} \cdot d\mathbf{T}^{-\top}(\mathbf{y}) \widehat{\nabla} \hat{w} - \kappa^2 \hat{v} \hat{w} \right) J(\mathbf{y}) \, d\hat{\mathbf{x}} \\ & - \kappa \int_{\Gamma_0} \hat{v} \hat{w} J_S(\mathbf{y}) \, ds_{\hat{\mathbf{x}}}, \quad \forall \hat{v}, \hat{w} \in H^1(D_0), \end{aligned} \quad (2.12)$$

and the anti-linear form $\widehat{\ell}(\cdot; \mathbf{y}) : H^1(D_0) \rightarrow \mathbb{C}$ is defined as

$$\widehat{\ell}(\widehat{v}; \mathbf{y}) := \int_{D_0} \widehat{f}(\mathbf{y}) \widehat{v} J(\mathbf{y}) d\widehat{\mathbf{x}} + \int_{\Gamma_0} \widehat{g}(\mathbf{y}) \gamma_{\Gamma_0} \widehat{v} J_S(\mathbf{y}) ds_{\widehat{\mathbf{x}}}, \quad \forall v \in H^1(D_0), \quad (2.13)$$

where $\widehat{f}(\mathbf{y}) := \Phi(\mathbf{y})f \in L^2(D_0)$ and $\widehat{g}(\mathbf{y}) := \Phi(\mathbf{y})g \in L^2(\Gamma_0)$.

One can readily see that the unique solvability of Problem 2.3 together with the properties of the plain pullback operator straightforwardly entail the well-posedness of Problem 2.4, and indeed it holds $\Phi(\mathbf{y})u(\mathbf{y}) = \widehat{u}(\mathbf{y})$ for each $\mathbf{y} \in U$, where $u(\mathbf{y}) \in H^1(D(\mathbf{y}))$ and $\widehat{u}(\mathbf{y}) \in H^1(D_0)$ are the unique solutions to Problems 2.3 and 2.4, respectively.

2.4.2. Discrete Full-Order Model for Helmholtz Impedance Problem. The well-posedness of the discrete problem with H^1 -conforming finite elements carries over from the case without domain parametrization. Hence, we will later use continuous Lagrangian FE defined on a suitable mesh of D_0 to approximate Problem 2.4. Consequently, the model presented in this section fits the general framework introduced in Section 2.1 and 2.2: the role of the Hilbert space V in Section 2.1 is played by the Sobolev space $H^1(D_0)$, the role of V_h by the continuous Lagrangian FE, and $\mathbf{g}(\cdot, \cdot; \mathbf{y}) = \widehat{\mathbf{a}}(\cdot, \cdot; \mathbf{y}) - \widehat{\ell}(\cdot; \mathbf{y})$ for each $\mathbf{y} \in U$, with $\widehat{\mathbf{a}}(\cdot, \cdot; \mathbf{y})$ as in (2.12) and $\widehat{\ell}(\cdot; \mathbf{y})$ as in (2.13).

Regarding the convergence of the full-order model for the Helmholtz impedance problem with respect to the discretization of the FE space, we have the following result: For each $\mathbf{y} \in U$ there exists $h_0(\mathbf{y})$ (i.e. depending on \mathbf{y}) such that for $h < h_0(\mathbf{y})$ it holds

$$\|\widehat{u}(\mathbf{y}) - \widehat{u}_h(\mathbf{y})\|_{H^1(D_0)} \leq C(\mathbf{y}) \inf_{v_h \in V_h} \|\widehat{u}(\mathbf{y}) - v_h\|_{H^1(D_0)},$$

for some $C(\mathbf{y}) > 0$, where $\widehat{u}_h(\mathbf{y})$ is solution to the following variational problem

$$\widehat{\mathbf{a}}(\widehat{u}_h(\mathbf{y}), \widehat{v}_h; \mathbf{y}) = \widehat{\ell}(\widehat{v}_h; \mathbf{y}), \quad \forall \widehat{v}_h \in V_h$$

As it is customary for variational problems satisfying Garding-type inequalities, a minimal level of resolution of the FE space is required to obtain quasi-optimality, and, therefore, convergence of the Galerkin method. It is important to point out that the minimal level of resolution $h_0(\mathbf{y})$ and $C(\mathbf{y})$, which in principle depend of the particular instance of $\mathbf{y} \in U$, can be made independent of $\mathbf{y} \in U$ by using a finite covering argument and the compactness of U .

2.5. The Maxwell Lossy Cavity Problem in Parametric Domains. As a second model problem, we consider a time-harmonic electromagnetic cavity problem with circular frequency $\omega > 0$ in a parametrically defined bounded, Lipschitz domain $D(\mathbf{y})$, for each $\mathbf{y} \in U$ as in (2.6).

For simplicity, we consider a constant complex domain conductivity σ as well as a constant complex dielectric permittivity ε and magnetic permeability μ . In addition, we also introduce the quantity $\Lambda := \omega^2 \varepsilon - \omega \sigma$. As in [2], we make the following assumptions: There exists $\vartheta \in [0, 2\pi)$ such that

$$\mu_b := \operatorname{Re} \{e^{i\vartheta} \mu^{-1}\} > 0 \quad \text{and} \quad \Lambda_b := \operatorname{Re} \{-e^{i\vartheta} \Lambda\} > 0. \quad (2.15)$$

Lastly, we assume a continuous source current density, i.e. for each $\mathbf{y} \in U$ we assume $\mathbf{J} \in \mathcal{C}^0(D(\mathbf{y}); \mathbb{C}^3)$.

In this simplified setting, let \mathbf{E} and \mathbf{H} be the complex-valued electric and magnetic fields, respectively. Maxwell equations in $D(\mathbf{y})$ read (see, e.g., [42])

$$\begin{cases} \nabla \times \mathbf{E} + \omega \mu \mathbf{H} & = 0 & \text{in } D(\mathbf{y}), \\ (\omega \varepsilon + \sigma) \mathbf{E} - \nabla \times \mathbf{H} & = -\omega \mathbf{J} & \text{in } D(\mathbf{y}). \end{cases}$$

By defining the quantity $\kappa^2 := \omega^2 \mu \varepsilon - \omega \mu \sigma$ and applying the curl operator to the first equation, we can reduce the system to

$$\nabla \times (\nabla \times \mathbf{E}) - \kappa^2 \mathbf{E} = -\omega \mu \mathbf{J} \quad \text{in } D(\mathbf{y}) \quad (2.16)$$

On the boundary, we assume perfect electrical conductor (PEC) boundary conditions

$$\gamma_d^\times \mathbf{E} = \mathbf{0} \quad \text{on } \Gamma(\mathbf{y}),$$

where γ_d^\times denotes the flipped tangential trace, i.e. $\gamma_d^\times \mathbf{E} := \gamma_d(\mathbf{n} \times \mathbf{E})$. Thus, only the tangential component electric field on the boundary of the domain vanishes.

We define $H(\text{curl}; D(\mathbf{y}))$ and $H_0(\text{curl}; D(\mathbf{y}))$ as

$$\begin{aligned} H(\text{curl}; D(\mathbf{y})) &:= \{\mathbf{u} \in L^2(D(\mathbf{y}))^3 \mid \nabla \times \mathbf{u} \in L^2(D(\mathbf{y}))^3\}, \\ H_0(\text{curl}; D(\mathbf{y})) &:= \{\mathbf{u} \in H(\text{curl}; D(\mathbf{y})) \mid \gamma_D^\times \mathbf{u} = 0\}, \end{aligned}$$

and we equip them with the norm

$$\|\mathbf{u}\|_{H(\text{curl}; D(\mathbf{y}))} := \|\mathbf{u}\|_{L^2(D(\mathbf{y}))} + \|\nabla \times \mathbf{u}\|_{L^2(D(\mathbf{y}))}.$$

The variational formulation of (2.16) on the physical domain $D(\mathbf{y})$ reads as follows.

Problem 2.5 (Maxwell Cavity Problem in $D(\mathbf{y})$). *For each $\mathbf{y} \in U$, we seek $\mathbf{E}(\mathbf{y}) \in H_0(\text{curl}; D(\mathbf{y}))$ such that*

$$\mathbf{a}(\mathbf{E}(\mathbf{y}), \mathbf{V}; \mathbf{y}) = \ell(\mathbf{V}; \mathbf{y}), \quad \forall \mathbf{V} \in H_0(\text{curl}; D(\mathbf{y}))$$

with the parameter-dependent sesquilinear form $\mathbf{a}(\cdot, \cdot; \mathbf{y}) : H_0(\text{curl}; D(\mathbf{y})) \times H_0(\text{curl}; D(\mathbf{y})) \rightarrow \mathbb{C}$ form

$$\mathbf{a}(\mathbf{V}, \mathbf{W}; \mathbf{y}) := \int_{D(\mathbf{y})} (\mu^{-1}(\nabla \times \mathbf{V}) \cdot (\nabla \times \overline{\mathbf{W}}) - \Lambda \mathbf{V} \cdot \overline{\mathbf{W}}) \, dx, \quad \forall \mathbf{V}, \mathbf{W} \in H_0(\text{curl}; D(\mathbf{y}))$$

and the parameter-dependent anti-linear form $\ell(\cdot; \mathbf{y}) : H_0(\text{curl}; D(\mathbf{y})) \rightarrow \mathbb{C}$

$$\ell(\mathbf{V}; \mathbf{y}) := -i\omega \int_{D(\mathbf{y})} \mathbf{J} \cdot \overline{\mathbf{V}} \, dx, \quad \mathbf{V} \in H_0(\text{curl}; D(\mathbf{y})),$$

where $\mathbf{J} \in \mathcal{C}^0(D(\mathbf{y}); \mathbb{C}^3)$.

Due to the assumptions in (2.15), we can apply the Lax-Milgram lemma to show the well-posedness of Problem 2.5. Indeed, for a fixed parameter $\mathbf{y} \in U$ and any $\mathbf{V} \in H_0(\text{curl}; D(\mathbf{y}))$ it holds

$$|\mathbf{a}(\mathbf{V}, \mathbf{V}; \mathbf{y})| \geq \min\{\mu_b, \Lambda_b\} \|\mathbf{V}\|_{H(\text{curl}; D(\mathbf{y}))}^2, \quad (2.17)$$

with μ_b, Λ_b as in (2.15).

Consequently, for each $\mathbf{y} \in U$ the sesquilinear $\mathbf{a}(\cdot, \cdot; \mathbf{y})$ is coercive according to (2.17). Observe that the coercivity constant does not depend on $\mathbf{y} \in U$. In addition, since both $\mathbf{a}(\cdot, \cdot; \mathbf{y})$ and $\ell(\cdot; \mathbf{y})$ are continuous the Lax-Milgram lemma applies, thus yielding well-posedness of Problem 2.5 for each $\mathbf{y} \in U$.

2.5.1. Maxwell Cavity Problem in the Reference Domain. One noteworthy difference to the Helmholtz problem is that we have to define the pullback operator $\Phi : V \rightarrow V_0$ differently. In fact, to preserve $H(\text{curl}; D)$ -conformity of the fields, we need to use the following domain transformation, defined for each $\mathbf{y} \in U$ as

$$\Phi(\mathbf{y})(\mathbf{v}) := d\mathbf{T}(\mathbf{y})^{-\top}(\mathbf{v} \circ \mathbf{T}(\mathbf{y})), \quad \forall \mathbf{v} \in V(\mathbf{y}).$$

As discussed in [19, Lemma 2.2], for each $\mathbf{y} \in U$ the pullback operator $\Phi(\mathbf{y})$ in (2.18) admits bounded extension $\Phi(\mathbf{y}) \in \mathcal{L}_{\text{iso}}(H(\text{curl}; \Omega(\boldsymbol{\mu})), H(\text{curl}; D(\mathbf{y})))$. In addition, for each $\mathbf{u} \in H(\text{curl}; D(\mathbf{y}))$ it holds that

$$\nabla \times (\Phi(\mathbf{y})\mathbf{u}) = \det(d\mathbf{T}(\mathbf{y})) d\mathbf{T}^{-1}(\mathbf{y}) ((\nabla \times \mathbf{u}) \circ \mathbf{T}(\mathbf{y})).$$

For ease of notation, let us also define the pullback of the current density $\mathbf{J}(\mathbf{y}) := \mathbf{J} \circ \mathbf{T}_y \in \mathcal{C}^0(D_0; \mathbb{C}^3)$. With the previous Lemma at hand, we can now state the nominal variational problem for the Maxwell cavity problem (cf. [2]).

Problem 2.6 (Maxwell Cavity Problem in the Reference Domain). *For each $\mathbf{y} \in \mathsf{U}$, we seek $\widehat{\mathbf{E}}(\mathbf{y}) \in H_0(\text{curl}; \mathsf{D}_0)$ such that*

$$\widehat{\mathbf{a}}(\widehat{\mathbf{E}}(\mathbf{y}), \widehat{\mathbf{V}}; \mathbf{y}) = \widehat{\ell}(\widehat{\mathbf{V}}; \mathbf{y}), \quad \forall \widehat{\mathbf{v}} \in H_0(\text{curl}; \mathsf{D}_0),$$

where the sesquilinear form $\widehat{\mathbf{a}}(\cdot, \cdot; \mathbf{y}) : H_0(\text{curl}; \mathsf{D}_0) \times H_0(\text{curl}; \mathsf{D}_0) \rightarrow \mathbb{C}$ is given by

$$\begin{aligned} \widehat{\mathbf{a}}(\widehat{\mathbf{u}}, \widehat{\mathbf{v}}; \mathbf{y}) &= \int_{\mathsf{D}_0} J(\mathbf{y})^{-1} \mu^{-1} (d\mathbf{T}(\mathbf{y})(\nabla \times \widehat{\mathbf{u}})) \cdot (d\mathbf{T}(\mathbf{y})(\nabla \times \widehat{\mathbf{v}})) \\ &\quad - \Lambda J(\mathbf{y}) d\mathbf{T}^{-\top}(\mathbf{y}) \widehat{\mathbf{u}} \cdot d\mathbf{T}^{-\top}(\mathbf{y}) \widehat{\mathbf{v}} d\widehat{\mathbf{x}} \end{aligned} \quad (2.19)$$

and, for each $\mathbf{y} \in \mathsf{U}$, the anti-linear form $\widehat{\ell}(\cdot; \mathbf{y}) : H_0(\text{curl}; \mathsf{D}_0) \rightarrow \mathbb{C}$ is given by

$$\widehat{\ell}(\widehat{\mathbf{v}}; \mathbf{y}) := -i\omega \int_{\mathsf{D}_0} J(\mathbf{y}) \mathbf{J}(\mathbf{y}) \cdot d\mathbf{T}^{-\top}(\mathbf{y}) \widehat{\mathbf{v}} d\widehat{\mathbf{x}}. \quad (2.20)$$

2.5.2. Discrete Full-Order Model for Maxwell Cavity Problem. The Maxwell cavity problem is approximated in an $H(\text{curl}; \cdot)$ -conforming fashion using Nédélec elements as described in the reference works [5, 20], and [42].

The model presented in this section fits the general framework introduced in Section 2.1 and 2.2: the role of the Hilbert space V in Section 2.1 is played by the space $H_0(\text{curl}; \mathsf{D}_0)$, the role of V_h by the curl-conforming Nédélec elements as discussed previously, whereas \mathbf{g} is replaced by $\mathbf{g}(\cdot, \cdot; \mathbf{y}) = \widehat{\mathbf{a}}(\cdot, \cdot; \mathbf{y}) - \widehat{\ell}(\cdot; \mathbf{y})$ for each $\mathbf{y} \in \mathsf{U}$, with $\widehat{\mathbf{a}}(\cdot, \cdot; \mathbf{y})$ as in (2.19) and $\widehat{\ell}(\cdot; \mathbf{y})$ as in (2.20).

Indeed, as a consequence of the assumption stated in (2.15) Cea's lemma holds as

$$\left\| \widehat{\mathbf{E}}(\mathbf{y}) - \widehat{\mathbf{E}}_h(\mathbf{y}) \right\|_{H^1(\mathsf{D}_0)} \leq C \inf_{v_h \in V_h} \left\| \widehat{\mathbf{E}}(\mathbf{y}) - v_h \right\|_{H^1(\mathsf{D}_0)},$$

where $\widehat{\mathbf{E}}_h(\mathbf{y}) \in V_h$ is the unique solution to the following variational problem

$$\widehat{\mathbf{a}}(\widehat{\mathbf{E}}_h(\mathbf{y}), \widehat{\mathbf{V}}_h; \mathbf{y}) = \widehat{\ell}(\widehat{\mathbf{V}}_h; \mathbf{y}), \quad \forall \widehat{\mathbf{V}}_h \in V_h.$$

3. PROJECTION-BASED REDUCED ORDER MODELING

The Galerkin approximation of the shape-parametric Helmholtz impedance and Maxwell lossy cavity problems, as presented in Sections 2.4 and 2.5, for each parametric input entails a high computational cost. For many-query applications or real-time computations, one needs a fast and accurate methodology to evaluate the parameter-to-solution map for each particular instance of the parametric input.

This motivates the use of model order reduction techniques such as the reduced basis method. Instead of seeking a solution for each parametric input in a suitable finite-dimensional subspace, we solve the problem in a reduced space of a much smaller dimension than that of the full-order model.

3.1. The Reduced Basis Method. Assume that we have access to a reduced basis $V_L^{(\text{rb})}$ of dimension $L \ll N_h$ of the form $V_L^{(\text{rb})} = \text{span}\{\psi_1, \dots, \psi_L\} \subset V_h$. We discuss one possible way to construct such a basis in Section 3.2. In practical applications one considers only finitely many parametric inputs. To this end, we define $\mathsf{U}^{(J)} := [-1, 1]^J$, where $J \in \mathbb{N}$ corresponds to the parametric dimension. Then, for a given parametric input $\mathbf{y} \in \mathsf{U}^{(J)}$, we seek solutions $u_L^{(\text{rb})}(\mathbf{y}) \in V_L^{(\text{rb})}$ of the form

$$u_L^{(\text{rb})}(\mathbf{y}) = \sum_{\ell=1}^L \left(\mathbf{u}_L^{(\text{rb})}(\mathbf{y}) \right)_\ell \psi_\ell \in V_L^{(\text{rb})},$$

with $\mathbf{u}^{(\text{rb})}(\mathbf{y}) \in \mathbb{C}^L$ being the *reduced coefficients*.

In order to compute the reduced basis solution $u_L^{(\text{rb})}(\mathbf{y})$ for a particular $\mathbf{y} \in \mathsf{U}^{(J)}$, we follow a standard Galerkin approach, see e.g. [48]. We project the variational problem (2.2) onto the

reduced space $V_L^{(\text{rb})}$, thus yielding the following *reduced basis problem*: Given $\mathbf{y} \in \mathcal{U}^{(J)}$, find $u_L^{(\text{rb})}(\mathbf{y}) \in V_L^{(\text{rb})}$ such that

$$\mathbf{g} \left(u_L^{(\text{rb})}(\mathbf{y}), v_L^{(\text{rb})}; \mathbf{y} \right) = 0, \quad \forall v_L^{(\text{rb})} \in V_L^{(\text{rb})}. \quad (3.1)$$

As in Section 2.2, each $\psi_\ell \in V_L^{(\text{rb})}$ can be uniquely represented by the sequence $\{c_m(\psi_\ell)\}_{m=1}^{N_h}$, which we gather in the vector $\boldsymbol{\psi}_\ell$. Next, we define the *reduced basis matrix* as

$$\mathbb{V}_L^{(\text{rb})} := (\boldsymbol{\psi}_1, \dots, \boldsymbol{\psi}_L) \in \mathbb{C}^{N_h \times L}.$$

This matrix encodes the change of basis from the reduced basis to the FE basis. Due to (2.3), the reduced basis problem (3.1) can be expressed as follows: Given $\mathbf{y} \in \mathcal{U}^{(J)}$, we seek $\mathbf{u}^{(\text{rb})}(\mathbf{y}) \in \mathbb{C}^L$ such that

$$\mathbb{V}_L^{(\text{rb})\dagger} \mathbf{G}_h \left(\mathbb{V}_L^{(\text{rb})} \mathbf{u}_L^{(\text{rb})}(\mathbf{y}); \mathbf{y} \right) = \mathbf{0} \in \mathbb{C}^L, \quad (3.2)$$

where \dagger denotes the Hermitian conjugate of $\mathbb{V}_L^{(\text{rb})}$. We will henceforth refer to (3.2) as the Galerkin-POD problem or simply G-POD.

Note that G-POD problem, although a system (either linear or non-linear) of L equations, still requires the assembly of the full-order model as described in [34, 48]. In special cases, e.g. whenever the dependence of the underlying form \mathbf{g} on the parametric input $\mathbf{y} \in \mathcal{U}$ is affine, it is possible that problem (3.2) turns out to be independent of N_h [48]. However, the Helmholtz problem as well as the time-harmonic Maxwell problem presented above do not satisfy this assumption.

3.2. Reduced Basis Construction: Proper Orthogonal Decomposition. A well-known and straightforward approach to construct a reduced basis is the *proper orthogonal decomposition* (POD) method. Suppose we have a collection of N_s evaluations of the full-order model on a finite parameter set $\Xi_{N_s} = \{\mathbf{y}^{(1)}, \dots, \mathbf{y}^{(N_s)}\} \subset \mathcal{U}^{(J)}$, the so-called snapshots $\{u_h(\mathbf{y}^{(1)}), \dots, u_h(\mathbf{y}^{(N_s)})\}$.

For what follows, we assume that a sufficiently large number of snapshots N_s have been computed so that the associated subspace

$$\mathcal{M}_\Xi := \text{span} \left\{ u_h(\mathbf{y}^{(1)}), \dots, u_h(\mathbf{y}^{(N_s)}) \right\} \subset V_h$$

is a good approximation of the continuous *solution manifold*

$$\mathcal{M}_h := \{u_h(\mathbf{y}) \mid \mathbf{y} \in \mathcal{U}^{(J)}\}. \quad (3.3)$$

Thus, we search for a parameter-independent reduced basis $\{\psi_1, \dots, \psi_L\}$ for \mathcal{M}_Ξ , such that $L \ll N_h$ and such that the reduced basis well approximates $\mathcal{M}_\Xi \subset \mathcal{M}_h$.

Let $\mathbb{S} \in \mathbb{C}^{N_h \times N_s}$ denote the *snapshot matrix*, defined as

$$\mathbb{S} := \left(\mathbf{u}_h(\mathbf{y}^{(1)}), \dots, \mathbf{u}_h(\mathbf{y}^{(N_s)}) \right) \in \mathbb{C}^{N_h \times N_s}. \quad (3.4)$$

Let R be the rank of \mathbb{S} . Then the singular value decomposition yields two unitary matrices

$$\mathbb{W} = (\mathbf{w}_1, \dots, \mathbf{w}_{N_s}) \in \mathbb{C}^{N_h \times N_h} \quad \text{and} \quad \mathbb{Z} = (\mathbf{z}_1, \dots, \mathbf{z}_{N_s}) \in \mathbb{C}^{N_s \times N_s}$$

and a diagonal matrix $\mathbb{D} = \text{diag}(\sigma_1, \dots, \sigma_R)$, with $\sigma_1 \geq \sigma_2 \geq \dots \geq \sigma_R > 0$, R being the rank of \mathbb{S} , such that

$$\mathbb{S} = \mathbb{W} \begin{pmatrix} \mathbb{D} & 0 \\ 0 & 0 \end{pmatrix} \mathbb{Z}^\dagger = \mathbb{W} \Sigma \mathbb{Z}^\dagger. \quad (3.5)$$

Algebraically speaking, we want to approximate the columns in \mathbb{S} using $L \leq R$ orthonormal vectors $\{\tilde{\mathbf{w}}_1, \dots, \tilde{\mathbf{w}}_L\}$. The orthogonal projection of $\mathbf{u}_h(\mathbf{y}^{(n)})$ onto $\text{span}\{\tilde{\mathbf{w}}_1, \dots, \tilde{\mathbf{w}}_L\}$ is given by

$$\sum_{l=1}^L \left(\mathbf{u}_h(\mathbf{y}^{(n)}), \tilde{\mathbf{w}}_l \right)_{\mathbb{C}^{N_h}} \tilde{\mathbf{w}}_l.$$

We seek an orthonormal basis $\{\tilde{\mathbf{w}}_1, \dots, \tilde{\mathbf{w}}_L\}$ such that the quantity

$$\tilde{\mathcal{E}}^{(N_s)}(\mathbb{V}_L) := \sum_{n=1}^{N_s} \left\| \mathbf{u}_h(\mathbf{y}^{(n)}) - \sum_{\ell=1}^L (\mathbf{u}_h(\mathbf{y}^{(n)}, \tilde{\mathbf{w}}_\ell)_{\mathbb{C}^{N_h}} \tilde{\mathbf{w}}_\ell \right\|_{\mathbb{C}^{N_h}}^2, \quad (3.6)$$

is minimized. The Schmidt-Eckart-Young theorem [48] asserts that the minimum is achieved for the basis $\{\mathbf{w}_1, \dots, \mathbf{w}_L\}$ consisting of the first L columns of \mathbb{W} in the SVD of \mathbb{S} in (3.5). Hence, we set $\boldsymbol{\psi}_l = \mathbf{w}_l$ for $l = 1, \dots, L$ and thus

$$\mathbb{V}_L^{(\text{rb})} = (\mathbf{w}_1, \dots, \mathbf{w}_L) \in \mathbb{C}^{N_h \times L}. \quad (3.7)$$

3.3. Parametric Holomorphy. In Sections 3.1 and 3.2 we have discussed computational aspects of the reduced basis method for parametric problems. The reduced basis method, and for that matter any other model order reduction technique, can successfully approximate the solution manifold \mathcal{M}_h defined in (3.3), and its discrete counterpart \mathcal{M}_Ξ , provided that there exists an intrinsic low-dimensional dynamics driving the behavior of solution manifold.

A commonly used concept in nonlinear approximation to quantify uniform error bounds is the so-called Kolmogorov's width. For a compact subset \mathcal{K} of a Banach space X it is defined for $L \in \mathbb{N}$ as

$$d_L(\mathcal{K}, X) := \inf_{\dim(X_L) \leq L} \sup_{v \in \mathcal{K}} \min_{w \in X_L} \|v - w\|_X,$$

where the outer infimum is taken over all finite dimensional spaces $X_L \subset X$ of dimension smaller than L . This quantifies the suitability of L -dimensional subspaces for the approximation of the solution manifold. As it has been established, see e.g. [34, 48] the convergence analysis of the reduced basis method relies on the existence of bounds controlling the decay of the Kolmogorov's width.

A key insight to establish dimension-independent convergence of Kolmogorov's width for parametric maps with high-dimensional parametric inputs corresponds to the analytic or holomorphic dependence of the parameter-to-operator map upon the parametric variables.

For $s > 1$ we define the Bernstein ellipse

$$\mathcal{E}_s := \left\{ \frac{z + z^{-1}}{2} : 1 \leq |z| \leq s \right\} \subset \mathbb{C}.$$

This ellipse has foci at $z = \pm 1$ and semi-axes of length $a := (s + s^{-1})/2$ and $b := (s - s^{-1})/2$. In addition, we define the tensorized poly-ellipse

$$\mathcal{E}_\boldsymbol{\rho} := \bigotimes_{j \geq 1} \mathcal{E}_{\rho_j} \subset \mathbb{C}^{\mathbb{N}},$$

where $\boldsymbol{\rho} := \{\rho_j\}_{j \geq 1}$ is such that $\rho_j > 1$, for $j \in \mathbb{N}$.

Definition 3.1 ([12, Definition 2.1]). *Let X be a complex Banach space equipped with the norm $\|\cdot\|_X$. For $\varepsilon > 0$ and $p \in (0, 1)$, we say that map $\mathbb{U} \ni \mathbf{y} \mapsto u(\mathbf{y}) \in X$ is $(\mathbf{b}, p, \varepsilon)$ -holomorphic if and only if:*

- (i) *The map $\mathbb{U} \ni \mathbf{y} \mapsto u(\mathbf{y}) \in X$ is uniformly bounded.*
- (ii) *There exists a positive sequence $\mathbf{b} := \{b_j\}_{j \geq 1} \in \ell^p(\mathbb{N})$ and a constant $C_\varepsilon > 0$ such that for any sequence $\boldsymbol{\rho} := \{\rho_j\}_{j \geq 1}$ of numbers strictly larger than one that is $(\mathbf{b}, \varepsilon)$ -admissible, i.e. satisfying $\sum_{j \geq 1} (\rho_j - 1)b_j \leq \varepsilon$, the map $\mathbf{y} \mapsto u(\mathbf{y})$ admits a complex extension $\mathbf{z} \mapsto u(\mathbf{z})$ that is holomorphic with respect to each variable z_j on a set of the form*

$$\mathcal{O}_\boldsymbol{\rho} := \bigotimes_{j \geq 1} \mathcal{O}_{\rho_j},$$

where $\mathcal{O}_{\rho_j} = \{z \in \mathbb{C} : \text{dist}(z, [-1, 1]) < \rho_j - 1\}$.

- (iii) *This extension is bounded on $\mathcal{E}_\boldsymbol{\rho}$ according to $\sup_{\mathbf{z} \in \mathcal{E}_\boldsymbol{\rho}} \|u(\mathbf{z})\|_X \leq C_\varepsilon$.*

The following result addresses the holomorphic dependence of the solution to both problems upon the parametric input.

Proposition 3.2 (Parametric Holomorphy of the Discrete Parameter-to-Solution Map). *Let Assumption 2.1 be satisfied with $p \in (0, 1)$ and $\mathbf{b} \in \ell^p(\mathbb{N})$.*

- (i) **Helmholtz Impedance Problem.** *The map $\mathcal{S}_{\text{Helmholtz}} : \mathbf{U} \rightarrow H^1(D_0) : \mathbf{y} \mapsto \widehat{u}_h(\mathbf{y})$ is $(\mathbf{b}, p, \varepsilon)$ -holomorphic for some $\varepsilon > 0$.*
- (ii) **Maxwell Lossy Cavity.** *The map $\mathcal{S}_{\text{Maxwell}} : \mathbf{U} \rightarrow H_0(\text{curl}; D_0) : \mathbf{y} \mapsto \widehat{\mathbf{E}}_h(\mathbf{y})$ is also $(\mathbf{b}, p, \varepsilon)$ -holomorphic for some $\varepsilon > 0$.*

In either case, $\varepsilon > 0$ does not depend on the Galerkin discretization parameter $h > 0$.

Proof. A complete proof of the first statement is included in Appendix A. The second statement has been proved in [2]. \square

Let us define the solution manifold for the discrete Helmholtz impedance and Maxwell lossy cavity problems as

$$\begin{aligned} \mathcal{M}_{\text{Helmholtz}} &:= \{ \widehat{u}_h(\mathbf{y}) \in H^1(D_0) : \mathbf{y} \in \mathbf{U} \}, \quad \text{and} \\ \mathcal{M}_{\text{Maxwell}} &:= \{ \widehat{\mathbf{E}}_h(\mathbf{y}) \in H_0(\text{curl}; D_0) : \mathbf{y} \in \mathbf{U} \}. \end{aligned} \quad (3.8)$$

As thoroughly discussed in [13], as a consequence of Proposition 3.2 we have the following result concerning the decay of Kolmogorov's width for the solution manifolds introduced in (3.8).

Lemma 3.3 (Decay of Kolmogorov's Width, [13]). *Let Assumption 2.1 be satisfied with $\mathbf{b} \in \ell^p(\mathbb{N})$ and $p \in (0, 1)$. Then, it holds*

$$\begin{aligned} d_L(\mathcal{M}_{\text{Helmholtz}}, H^1(D_0)) &\leq C(L+1)^{-\left(\frac{1}{p}-1\right)} \quad \text{and} \\ d_L(\mathcal{M}_{\text{Maxwell}}, H_0(\text{curl}; D_0)) &\leq C(L+1)^{-\left(\frac{1}{p}-1\right)}, \end{aligned}$$

for some constant $C > 0$ independent of $L \in \mathbb{N}$.

3.4. Convergence of the Galerkin-POD RB Method. In Section 3.3 we established the holomorphic dependence of the solution to both the Helmholtz interior impedance and Maxwell lossy cavity problems upon the parametric variables describing the problems' shape deformations. Among the consequences of this property, and relevant for subsequent developments, we have the approximability of the solution manifolds defined in (3.8) through finite dimensional linear subspaces. This property is reflected in terms of the dimension-independent decay of Kolmogorov's width as described in Lemma 3.3.

Using the properties of the solution manifold described in Section 3.3, and following the presentation of [34, 48], we are interested in establishing dimension-independent convergence rates of the Galerkin-POD-RB method.

To this end, we observe that the $(\mathbf{b}, p, \varepsilon)$ -holomorphy of the parameter-to-solution map implies $u_h \in L^2(\mathbf{U}^{(J)}; V_h)$, thus u_h is a Hilbert-Schmidt kernel and $\mathbb{T} : L^2(\mathbf{U}^{(J)}) \rightarrow V_h$ defined as

$$\mathbb{T}g = \int_{\mathbf{U}^{(J)}} u_h(\mathbf{y})g(\mathbf{y}) \, d\mathbf{y}, \quad g \in L^2(\mathbf{U}^{(J)}),$$

is a compact Hilbert-Schmidt operator with adjoint $\mathbb{T}^\dagger : V_h \rightarrow L^2(\mathbf{U}^{(J)})$ admitting for each $\mathbf{y} \in \mathbf{U}$ the following expression $(\mathbb{T}^\dagger v_h)(\mathbf{y}) = (u_h(\mathbf{y}), v_h)_V \quad \forall v_h \in V_h$. As a consequence, the operators $\mathbb{K} := \mathbb{T}\mathbb{T}^\dagger : V_h \rightarrow V_h$ and $\mathbb{C} := \mathbb{T}^\dagger\mathbb{T} : L^2(\mathbf{U}^{(J)}) \rightarrow L^2(\mathbf{U}^{(J)})$ are Hermitian, non-negative, and compact. The latter operator can be represented by the matrix

$$\mathbf{K}_h = \int_{\mathbf{U}^{(J)}} \mathbf{u}_h(\mathbf{y})\mathbf{u}_h(\mathbf{y})^\dagger \, d\mathbf{y} \in \mathbb{C}^{N_h \times N_h}.$$

Let $\sigma_1^2 \geq \dots \geq \sigma_r^2 > 0$ be the eigenvalues of \mathbf{K}_h , with $r = \text{rank}(\mathbf{K}_h)$, associated to the eigenvectors ζ_1, \dots, ζ_r , respectively, i.e. $\mathbf{K}_h \zeta_i = \sigma_i^2 \zeta_i$, $i = 1, \dots, r$. Let us set for $i = 1, \dots, r$

$$\zeta_{i,h} = \sum_{j=1}^{N_h} (\zeta_i)_j \varphi_j \in V_h \quad \text{and} \quad V_L^{(\text{rb})} = \text{span} \{ \zeta_{1,h}, \dots, \zeta_{r,h} \},$$

Then, according to [48, Proposition 6.3], it holds

$$V_L^{(\text{rb})} = \arg \min_{\substack{V_L \subset V_h \\ \dim(V_L) \leq L}} \|u_h - \mathbf{P}_{V_L} u_h\|_{L^2(\mathbf{U}^{(J)}; V)}^2. \quad (3.9)$$

For each $\mathbf{y} \in \mathbf{U}^{(J)}$, we are interested in finding $u_L^{(\text{rb})}(\mathbf{y}) \in V_L^{(\text{rb})}$ such that

$$\mathbf{a}(u_L^{(\text{rb})}(\mathbf{y}), v_L^{(\text{rb})}; \mathbf{y}) = \ell(v_L^{(\text{rb})}; \mathbf{y}), \quad \forall v_L^{(\text{rb})} \in V_L^{(\text{rb})}. \quad (3.10)$$

In the following, we refer to $\widehat{u}_L^{(\text{rb})}$ and $\widehat{\mathbf{E}}_L^{(\text{rb})}$ as the solution of (3.10) when considering the reduced counterparts of the discrete Helmholtz impedance and the Maxwell cavity problems as described in Subsection 2.4.2 and 2.5.2, respectively.

Theorem 3.4 (Convergence of the Galerkin-POD RB Method). *Let Assumption 2.1 be satisfied with $p \in (0, 1)$ and $\mathbf{b} \in \ell^p(\mathbb{N})$.*

- (i) **Helmholtz Impedance Problem.** *There exists $L_0 \in \mathbb{N}$ such that there exists $C > 0$ such that for each $L \geq L_0$ and any $J \in \mathbb{N}$ it holds*

$$\left\| \widehat{u}_h - \widehat{u}_L^{(\text{rb})} \right\|_{L^2(\mathbf{U}^{(J)}; H^1(\mathbf{D}_0))} \leq C(L+1)^{-\left(\frac{1}{p}-1\right)}.$$

- (ii) **Maxwell Lossy Cavity.** *There exists $C > 0$ and $L_0 \in \mathbb{N}$ such that for each $L \in \mathbb{N}$ and any $J \in \mathbb{N}$*

$$\left\| \widehat{\mathbf{E}}_h - \widehat{\mathbf{E}}_L^{(\text{rb})} \right\|_{L^2(\mathbf{U}^{(J)}; H_0(\text{curl}; \mathbf{D}_0))} \leq C(L+1)^{-\left(\frac{1}{p}-1\right)}.$$

Proof. Firstly, we consider the Helmholtz interior impedance problem. Similarly as for the discrete Helmholtz full order model described in 2.4.2, the application of Cea's Lemma (which in principle is valid for any finite dimensional subspace) yields for each $\mathbf{y} \in \mathbf{U}$ and $L \geq L_0$

$$\left\| \widehat{u}_h(\mathbf{y}) - \widehat{u}_L^{(\text{rb})}(\mathbf{y}) \right\|_{H^1(\mathbf{D}_0)} \leq C \inf_{v_L \in V_L^{(\text{rb})}} \|\widehat{u}_h(\mathbf{y}) - v_L\|_{H^1(\mathbf{D}_0)},$$

where $C > 0$ is a uniform constant and a minimal level of refinement L_0 of the reduced space is required. The final assertion follows from Lemma 3.3 and (3.9). The assertion for the Maxwell cavity problem follows from the exact same arguments, however no base level of refinement of the reduced space is required due to the ellipticity of the corresponding sesquilinear form, i.e. (2.17). \square

3.5. Snapshot Selection. The results presented rely in Section 3.4 on the assumption that the reduced basis $V_L^{(\text{rb})}$ can be computed as in (3.9), which in turn implies the exact computation of an integral over the parameter space $\mathbf{U}^{(J)}$. Even after considering only the first J parametric dimensions, this integral needs to be approximated by a suitable quadrature rule in $\mathbf{U}^{(J)} := [-1, 1]^J$, as discussed, e.g., in [48, Section 6.5]. The quadrature points define the set Ξ_{N_s} introduced in Section 3.2 for the computation of the snapshots. The effect of the truncation in the parametric dimension yields as error term decaying as $J^{-\left(\frac{1}{p}-1\right)}$.

Consider the general framework introduced in Section 2.2. For a finite dimensional subspace $V_L = \text{span}\{v_1, \dots, v_L\} \subset V_h$ we set

$$\mathcal{E}(V_L) = \|u_h - \mathbf{P}_{V_L} u_h\|_{L^2(\mathbf{U}^{(J)}; V)}^2 \quad \text{and} \quad \mathcal{E}^{(N_s)}(V_L) = \frac{1}{N_s} \sum_{i=1}^{N_s} \left\| u_h(\mathbf{y}^{(i)}) - \mathbf{P}_{V_L} u_h(\mathbf{y}^{(i)}) \right\|_V^2,$$

where the latter is an N_s -points, equal weights, J -dimensional quadrature rule with quadrature points $\{\mathbf{y}^{(1)}, \dots, \mathbf{y}^{(N_s)}\} \subset \mathbb{U}^{(J)}$ which approximates $\mathcal{E}(V_R)$. As in [48, Section 6.5], we decompose the error as follows

$$\mathcal{E}(V_L) \leq \underbrace{\left| \mathcal{E}(V_L) - \mathcal{E}^{(N_s)}(V_L) \right|}_{\text{Quadrature Error}} + \mathcal{E}^{(N_s)}(V_L) \quad (3.11)$$

Furthermore, as we are working in a finite dimensal subspace V_h , one has

$$\mathcal{E}^{(N_s)}(V_L) \cong \tilde{\mathcal{E}}^{(N_s)}(\mathbb{V}_L),$$

where the hidden constants depend on V_h , $\mathbb{V}_L = (\mathbf{v}_1, \dots, \mathbf{v}_L) \in \mathbb{C}^{N_h \times L}$, v_j and \mathbf{v}_j are connected as described in (2.4), and $\tilde{\mathcal{E}}^{(N_s)}$ is as in (3.6).

The quadrature error in (3.11) depends on the problem's parametric dimension. The parametric domain deformations considered in this work, as described in Section 2.3, allowing high-dimensional parametric inputs controlling the domain's shape deformations.

In the following, we consider low discrepancy sequences as quadrature rules. For a specific definition we refer to [7]. Examples of low-discrepancy sequences include those of Sobol' [52], Halton [25], and Owen [45]. In [40, 41], low-discrepancy sequences have been considered for the generation of training data in the approximation of quantities of interested by means of NNs. The exact same principle applies for the approximation of the quadrature error in (3.11). Indeed, as in [41, Lemma 3.4] one can show that

$$\left| \mathcal{E}(V_L) - \mathcal{E}^{(N_s)}(V_L) \right| \leq C V_{\text{HK}} \frac{(\log N_s)^J}{N_s},$$

for a constant $C > 0$, where V_{HK} corresponds to the Hardy-Krause variation of the map $\mathbb{U}^{(J)} \ni \mathbf{y} \mapsto \|u_h(\mathbf{y}) - P_{V_L} u_h(\mathbf{y})\|_V^2 \in \mathbb{R}$. Therefore, we may conclude that for $\mathbb{V}_L^{(\text{rb})}$ as in (3.7) and with $V_L^{(\text{rb})}$ being the representation of this basis in the FE space V_h , together with 3.11 we have

$$\mathcal{E}(V_L^{(\text{rb})}) \lesssim V_{\text{HK}} \frac{(\log N_s)^J}{N_s} + \sum_{j=L+1}^R \sigma_j^2,$$

where $\sigma_j > 0$ are the singular values of the snapshot matrix \mathbb{S} defined in (3.4).

3.6. Centered RB-POD Implementation. As in [10], we consider a construction of the reduced basis in the following referred to as the *centered RB-POD*. Provided snapshots $\mathbf{s}_1, \dots, \mathbf{s}_{N_s} \in \mathbb{C}^{N_s}$, we define the mean of the snapshots as

$$\bar{\mathbf{u}} := \frac{1}{N_s} \sum_{n=1}^{N_s} \mathbf{u}_h(\mathbf{y}^{(n)}) \in \mathbb{C}^{N_h}.$$

Let \mathbb{S} be the snapshot matrix as in (3.4), set $\bar{\mathbb{S}} = (\bar{\mathbf{u}}, \dots, \bar{\mathbf{u}}) \in \mathbb{C}^{N_h \times N_s}$, and consider the SVD of $\mathbb{S} - \bar{\mathbb{S}}$

$$\mathbb{S} - \bar{\mathbb{S}} = \bar{\mathbb{W}} \begin{pmatrix} \bar{\mathbb{D}} & 0 \\ 0 & 0 \end{pmatrix} \bar{\mathbb{Z}}^\dagger = \bar{\mathbb{W}} \bar{\Sigma} \bar{\mathbb{Z}}^\dagger.$$

with $R = \text{rank}(\mathbb{S} - \bar{\mathbb{S}})$, $\bar{\mathbb{D}} \in \mathbb{R}^{R \times R}$ a diagonal matrix containing the singular values of $\mathbb{S} - \bar{\mathbb{S}}$, and

$$\bar{\mathbb{W}} = (\bar{\mathbf{w}}_1, \dots, \bar{\mathbf{w}}_{N_s}) \in \mathbb{C}^{N_h \times N_h} \quad \text{and} \quad \bar{\mathbb{Z}} = (\bar{\mathbf{z}}_1, \dots, \bar{\mathbf{z}}_{N_s}) \in \mathbb{C}^{N_s \times N_s}.$$

We set

$$\bar{\mathbb{V}}_L^{(\text{rb})} = (\bar{\mathbf{w}}_1, \dots, \bar{\mathbf{w}}_L) \in \mathbb{C}^{N_h \times L}.$$

We look for a reduced solution to (3.2) of the form $\bar{\mathbb{V}}_L^{(\text{rb})} \bar{\mathbf{u}}_L^{(\text{rb})}(\mathbf{y}) + \bar{\mathbf{u}}$, thus yielding the following problem: For each $\mathbf{y} \in \mathbb{U}^{(J)}$, we seek $\bar{\mathbf{u}}_L^{(\text{rb})} \in \mathbb{C}^L$ such that

$$\bar{\mathbb{V}}_L^{(\text{rb})\dagger} \mathbf{G}_h \left(\bar{\mathbb{V}}_L^{(\text{rb})} \bar{\mathbf{u}}_L^{(\text{rb})}(\mathbf{y}) + \bar{\mathbf{u}}; \mathbf{y} \right) = \mathbf{0} \in \mathbb{C}^L,$$

which in the linear case amounts to adapting the RHS of the system, as follows

$$\overline{\mathbb{V}}_L^{(\text{rb})\dagger} \mathbf{G}_h(\mathbf{y}) \overline{\mathbb{V}}_L^{(\text{rb})} \overline{\mathbf{u}}_L^{(\text{rb})}(\mathbf{y}) = -\overline{\mathbb{V}}_L^{(\text{rb})\dagger} \mathbf{G}_h(\mathbf{y}) \overline{\mathbf{u}}.$$

4. GALERKIN POD - NEURAL NETWORK

In this section, we introduce the Galerkin POD Neural Network (POD-NN) as proposed in [33] and propose minor modifications to accommodate the complex-valued nature of the solutions. We further formulate the learning problem centered around the mean, which facilitates the learning task for the NN.

4.1. Neural Networks. In this work, we consider multi-layer perceptron architectures consisting of $D \in \mathbb{N}$ layers, with layer width $\ell_0, \dots, \ell_D \in \mathbb{N}$. The activation function $\sigma : \mathbb{R} \rightarrow \mathbb{R}$ may be chosen as any nonlinear function, we restrict our discussion to the hyperbolic tangent defined as

$$\sigma(x) = \tanh(x) = \frac{\exp(x) - \exp(-x)}{\exp(x) + \exp(-x)}, \quad x \in \mathbb{R}.$$

Given weights and biases $\boldsymbol{\theta} := (\mathbf{W}_k, \mathbf{b}_k)_{k=1}^D$, $\mathbf{W}_k \in \mathbb{R}^{\ell_k \times \ell_{k-1}}$, $\mathbf{b}_k \in \mathbb{R}^{\ell_k}$, we define the affine transformation $\mathbf{A}_k : \mathbb{R}^{\ell_{k-1}} \rightarrow \mathbb{R}^{\ell_k} : \mathbf{x} \mapsto \mathbf{W}_k \mathbf{x} + \mathbf{b}_k$ for $k \in \{1, \dots, D\}$. We may then define a neural network with activation function σ as a map $\Psi_{\boldsymbol{\theta}}^{\text{NN}} : \mathbb{R}^{\ell_0} \rightarrow \mathbb{R}^{\ell_D}$ with

$$\Psi_{\boldsymbol{\theta}}^{\text{NN}}(\mathbf{x}) := \begin{cases} \mathbf{A}_1(\mathbf{x}), & D = 1, \\ (\mathbf{A}_L \circ \sigma \circ \mathbf{A}_{L-1} \circ \sigma \cdots \circ \sigma \circ \mathbf{A}_1)(\mathbf{x}), & D \geq 2, \end{cases}$$

where the activation function $\sigma : \mathbb{R} \rightarrow \mathbb{R}$ is applied component-wise to vector-valued inputs. We define the depth and the width of an NN as

$$\text{width}(\Psi_{\boldsymbol{\theta}}^{\text{NN}}) = \max\{\ell_0, \dots, \ell_D\} \quad \text{and} \quad \text{depth}(\Psi_{\boldsymbol{\theta}}^{\text{NN}}) = D.$$

We denote by $\mathcal{NN}_{D,H,\ell_0,\ell_D}$ the set of all NNs $\Psi_{\boldsymbol{\theta}}^{\text{NN}}(\mathbf{x}) : \mathbb{R}^{\ell_0} \rightarrow \mathbb{R}^{\ell_D}$ with input dimension ℓ_0 , output dimension ℓ_D , a width of at most H , and a depth of at most D layers.

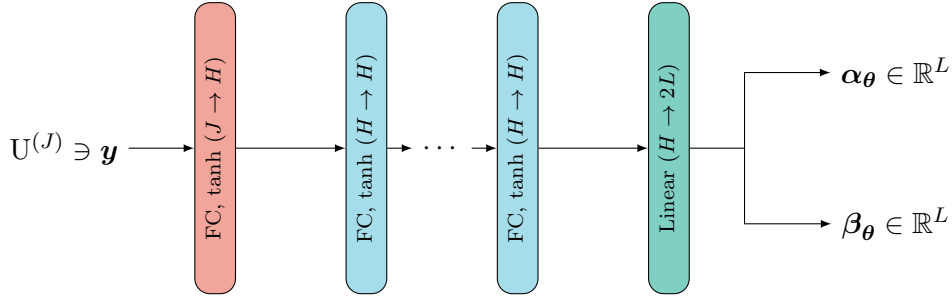


FIGURE 1. NN architecture for the approximation of the map $\pi_{L,\mathbb{R}}^{(\text{rb})} : \mathbb{U}^{(J)} \rightarrow \mathbb{R}^{2L}$ as in (4.2). The NN accepts as input J values accounting for the components of the parametric input $\mathbf{y} = (y_1, \dots, y_J) \in \mathbb{U}^{(J)}$, whereas there are $2L$ outputs representing both the real and imaginary parts of the reduced coefficients. The input (red) and hidden layers (blue) are fully connected (FC) with hyperbolic tangent (tanh) activation functions.

4.2. Formulation of the Learning Problem. Following the centered RB construction described in Section 3.6, we would like to approximate the parametric map

$$\pi_L^{(\text{rb})} : \mathbb{U}^{(J)} \rightarrow \mathbb{C}^L : \mathbf{y} \mapsto \mathbb{V}_L^{(\text{rb})\dagger} (\mathbf{u}_h(\mathbf{y}) - \overline{\mathbf{u}}), \quad (4.1)$$

by an NN, where $L \in \mathbb{N}$ is the dimension of the reduced space $\mathbb{V}_L^{(\text{rb})}$.

The map introduced in (4.1) has an output that is complex-valued, as the reduced coefficients are complex-valued themselves. However, this does not fit the NN definition stated in Section 4.1. Consequently, we proceed to formulate an equivalent real-valued learning problem.

Then, instead of approximating the map $\pi_L^{(\text{rb})}$ as in (4.1), we consider the map

$$\pi_{L,\mathbb{R}}^{(\text{rb})} : \mathbb{U}^{(J)} \rightarrow \mathbb{R}^{2L} : \mathbf{y} \mapsto \begin{pmatrix} \boldsymbol{\alpha}(\mathbf{y}) \\ \boldsymbol{\beta}(\mathbf{y}) \end{pmatrix} := \begin{pmatrix} \text{Re} \left\{ \mathbb{V}_L^{(\text{rb})\dagger} (\mathbf{u}_h(\mathbf{y}) - \bar{\mathbf{u}}) \right\} \\ \text{Im} \left\{ \mathbb{V}_L^{(\text{rb})\dagger} (\mathbf{u}_h(\mathbf{y}) - \bar{\mathbf{u}}) \right\} \end{pmatrix}, \quad (4.2)$$

$\boldsymbol{\alpha}(\mathbf{y}), \boldsymbol{\beta}(\mathbf{y}) \in \mathbb{R}^L$ for each $\mathbf{y} \in \mathbb{U}^{(L)}$, which returns separately the real and imaginary parts of the reduced coefficients in a real-valued vector of size $2L$.

Given a data set consisting of N_s training inputs $\mathbf{y}^{(i)} \in \mathbb{U}^{(J)}$, $i = 1, \dots, N_s$ and the corresponding high-fidelity snapshots $\mathbf{u}_h(\mathbf{y}^{(i)})$, $i = 1, \dots, N_s$, we can train an NN $\pi_{\boldsymbol{\theta}}^{(\text{rb})} \in \mathcal{NN}_{H,D,J,2L}$ (as in Section 4.1), i.e. with J inputs (one for each component of the parametric input $\mathbf{y} \in \mathbb{U}$, $2L$ outputs accounting for the L complex reduced coefficients, and depth and width D and H , respectively, on the set of training input-output pairs $\mathcal{P}_{\text{Train}} = \left\{ \left(\mathbf{y}^{(i)}, \pi_{L,\mathbb{R}}^{(\text{rb})}(\mathbf{y}^{(i)}) \right) \right\}_{1 \leq i \leq N_s}$. Figure 1 portrays the previously described architecture. The first L outputs emulate the real part of the reduced coefficients, whereas the second L outputs account for the imaginary one.

The mean square error (MSE) is a natural candidate for a loss function. More precisely, let $\boldsymbol{\theta}$ denote the vector gathering all weights and biases of the NN $\pi_{\boldsymbol{\theta}}^{(\text{rb})}$. Then, the MSE loss is given by

$$\begin{aligned} L_{\text{MSE}}(\boldsymbol{\theta}) &:= \frac{1}{N_s} \sum_{i=1}^{N_s} \left\| \pi_{L,\mathbb{R}}^{(\text{rb})}(\mathbf{y}^{(i)}) - \pi_{\boldsymbol{\theta}}^{(\text{rb})}(\mathbf{y}^{(i)}) \right\|_2^2 \\ &= \frac{1}{N_s} \sum_{i=1}^{N_s} \sum_{l=1}^L \left| \alpha_l(\mathbf{y}^{(i)}) - \alpha_{l,\boldsymbol{\theta}}(\mathbf{y}^{(i)}) \right|^2 + \left| \beta_l(\mathbf{y}^{(i)}) - \beta_{l,\boldsymbol{\theta}}(\mathbf{y}^{(i)}) \right|^2, \end{aligned} \quad (4.3)$$

where the outputs of the NN $\pi_{\boldsymbol{\theta}}^{(\text{rb})}$ are organized as follows (cp. Figure 1)

$$\pi_{\boldsymbol{\theta}}^{(\text{rb})}(\mathbf{y}) = (\boldsymbol{\alpha}_{\boldsymbol{\theta}}(\mathbf{y})^\top, \boldsymbol{\beta}_{\boldsymbol{\theta}}(\mathbf{y})^\top)^\top, \quad \mathbf{y} \in \mathbb{U}^{(J)}.$$

Let $\boldsymbol{\theta}^*$ be such that

$$\boldsymbol{\theta}^* \in \arg \min_{\boldsymbol{\theta}} L_{\text{MSE}}(\boldsymbol{\theta}).$$

Then, the reduced basis solution lifted to the original FEM space can be reconstructed as follows

$$\mathbf{u}^{\mathcal{NN}}(\mathbf{y}) := \overline{\mathbb{V}}_L^{(\text{rb})} (\boldsymbol{\alpha}_{\boldsymbol{\theta}^*}(\mathbf{y}) + i\boldsymbol{\beta}_{\boldsymbol{\theta}^*}(\mathbf{y})) + \bar{\mathbf{u}} \in \mathbb{C}^{N_h}, \quad \mathbf{y} \in \mathbb{U}^{(J)}.$$

4.3. Approximation Rates of the Galerkin POD-NN. The Galerkin POD-NN as originally described in [33] falls in a ever-increasing body of work usually referred to as *operator learning*. In particular, a thorough study of the Galerkin POD-NN has been performed in [38].

The following results claim that by separating the real and imaginary of the reduced coefficients does not break the parametric holomorphy property. Indeed, this is of key importance in establishing dimension-independent emulation rates for the reduced coefficients.

Lemma 4.1. *Let Assumption 2.1 be satisfied with $\mathbf{b} \in \ell^p(\mathbb{N})$ and $p \in (0, 1)$. There exists $J_0 \in \mathbb{N}$ such that for $J \geq J_0$ and for each $\mathbf{y} \in \mathbb{U}$ there exists a unique $u_L^{(\text{rb})}(\mathbf{y}) \in V_L^{(\text{rb})}$ solution to (3.10). In addition, the map $\pi_{L,\mathbb{R}}^{(\text{rb})} : \mathbb{U} \rightarrow \mathbb{R}^{2L}$ is $(\mathbf{b}, p, \varepsilon)$ -holomorphic.*

Proof. As in the proof of Proposition 3.2, we can argue that the maps

$$\mathbb{U} \ni \mathbf{y} \mapsto \widehat{u}_h(\mathbf{y}) \in H^1(D_0) \quad \text{and} \quad \mathbb{U} \ni \mathbf{y} \mapsto \widehat{\mathbf{E}}_h(\mathbf{y}) \in H_0(\text{curl}; D_0).$$

are $(\mathbf{b}, p, \varepsilon)$ -holomorphic, therefore the parameter-to-reduced coefficients are so as well. We observe that as in the proof of Proposition 3.2 a minimal level of refinement $h_0 > 0$ is required for this to hold for the Helmholtz impedance problem, and so is the case for the discretization in the reduced space.

As pointed out previously, for the sake of the implementation, the real and imaginary parts of these maps are approximated separately. However, the application of either the real or imaginary parts to a complex input is not an holomorphic map itself. Therefore, one can not

argue that the compositions of these maps yields an holomorphic one. In [18, Lemma A.1], it is proved that both the real and imaginary parts of complex-valued holomorphic function preserve this property, thus yielding the desired result. \square

Equipped with this result, together with [18, Lemma 2.6] which in turn follows from [1], we may the following approximation result of the Galerkin POD-NN.

Lemma 4.2. *Let Assumption 2.1 be satisfied with $\mathbf{b} \in \ell^p(\mathbb{N})$ and $p \in (0, 1)$. In addition, assume that \mathbf{b} is strictly decreasing. For each $n \in \mathbb{N}$ there exists a sequence of tanh NN $\Psi_{\mathcal{NN}}^{(n)} \in \mathcal{NN}_{D,H,J,2L}$ and $C > 0$ such that*

$$\left\| \boldsymbol{\pi}_{L,\mathbb{R}}^{(\text{rb})} - \Psi_{\mathcal{NN}}^{(n)} \right\|_{L^2(\mathcal{U}^{(J)}; \mathbb{R}^{2L})} \leq C n^{-\left(\frac{1}{p} - \frac{1}{2}\right)}$$

with $D = \mathcal{O}(n^2)$ and $H = \mathcal{O}(\log_2(n))$.

5. NUMERICAL EXPERIMENTS

5.1. Numerical implementation. We use the programming language Julia to conduct our numerical experiments. The high-fidelity FE methods for solving the Helmholtz impedance and Maxwell lossy cavity problem are implemented in `Gridap.jl` [3] using Lagrange and Nédélec elements, respectively. After assembly, the linear system is solved by Julia's native linear solver. For the boundary variations, the parameter space of the affine transformations is sampled using a Halton or Latin Hypercube sequence generated by the library `QuasiMonteCarlo.jl`. To compute the solution of the Galerkin-POD method, the linear operators are first assembled in `Gridap.jl`, then projected onto the reduced basis, and solved. The neural network architectures and training implementation are based on the library `Flux.jl` [36].

5.2. Performance evaluation. As in [33], we consider the following *relative* error measures with respect to a high-fidelity solution $\mathbf{u}_h(\mathbf{y})$ to assess the performance of a model:

- (i) the G-POD relative error

$$\mathcal{E}_G(L, \mathbf{y}) := \frac{\left\| \mathbf{u}_h(\mathbf{y}) - \left(\overline{\nabla}_L^{(\text{rb})} \overline{\mathbf{u}}_L^{(\text{rb})}(\mathbf{y}) + \overline{\mathbf{u}} \right) \right\|}{\left\| \mathbf{u}_h(\mathbf{y}) \right\|},$$

- (ii) the POD-NN relative error

$$\mathcal{E}_{\text{NN}}(L, \mathbf{y}) := \frac{\left\| \mathbf{u}_h(\mathbf{y}) - \left(\overline{\nabla}_L^{(\text{rb})} (\boldsymbol{\alpha}_\theta(\mathbf{y}) + \imath \boldsymbol{\beta}_\theta(\mathbf{y})) + \overline{\mathbf{u}} \right) \right\|}{\left\| \mathbf{u}_h(\mathbf{y}) \right\|},$$

- (iii) the relative projection error, i.e. the relative error between the reconstruction of the projection of a high-fidelity solution and itself

$$\mathcal{E}_V(L, \mathbf{y}) := \frac{\left\| \mathbf{u}_h(\mathbf{y}) - \left(\overline{\nabla}_L^{(\text{rb})} (\mathbf{u}_h(\mathbf{y}) - \overline{\mathbf{u}}) + \overline{\mathbf{u}} \right) \right\|}{\left\| \mathbf{u}_h(\mathbf{y}) \right\|}$$

Clearly, the latter error is a lower bound to the first two. To analyze the global performance of the model, the averages of the above error measures over test set are considered.

5.3. Numerical Results for the Helmholtz Impedance Problem. We test our implementation on the Helmholtz problem across different hyperparameter settings. We impose impedance boundary conditions as defined in (2.7). The following parameter choices are our standard setting unless specified otherwise. The wave number is set to $\kappa = 1$, and the boundary variation is parametrized with the Matérn-like decay, with $\nu = 0.5$, $l = 0.1$, $\theta = 0.1$, and parameter dimension $J = 50$. Figure 2 (a) and (b) show the original mesh on the unit cube, as well as a typical deformation of the boundary and domain. We sample 1024 snapshots from a Halton sequence for the construction of the reduced basis and the training of the network. To obtain an unbiased test set, we sample 512 snapshots from a Latin Hypercube sampling, which is used to evaluate the error measures introduced in the previous section, so that we avoid any positive biases between training and test set.

The NN baseline architecture comprises $D = 2$ hidden layers with $H = 30$ neurons and the tanh activation function. The network parameters are trained on the loss in equation (4.3) for 4000 epochs with the ADAM optimizer using a learning rate of $5e - 4$. Figure 2 (c) and (d) show the high-fidelity and POD-NN solution, respectively, depicting no visible differences between the two.

Figure 3 shows the scaling coefficients for the parameters in the 50-dimensional space, particularly the differences between the algebraic and Matérn-like decay. When computing the POD on the assembled snapshot matrix, we further observe that the decay of the singular values (see Figure 4) qualitatively follows the trend of the parameter decay. As expected, the fastest algebraic decay $r=3$, also leads to the fastest decay in singular values, while those of the Matérn case decay more slowly. We can thus confirm that an efficient RB construction with a limited basis size is possible for all domain mappings under consideration, which aligns with our theoretical statements in Section 3.

In Figure 5, we assess the test error for different NN architectures and vary the number of modes L in the RB basis. In all figures, we also report the error with zero basis functions ($L=0$), i.e. the error of using the mean field as a predictor. For the standard setting, we observe that the mean field already leads to a low relative error of $3e-4$, indicating that the parametric variation in this case is limited. Nevertheless, the best POD-NN architecture further reduces this error by an order of magnitude to $3e-5$. We further observe that increasing the depth of the NN does not lead to performance gains. Increasing the width does reduce the error further, but we observe a growth in error after more than 20 basis functions are added for all architectures. The increase in error is likely due to the fact that the learning problem becomes more difficult by adding more modes, as more RB coefficients need to be approximated: we have verified, that the error increase does not occur when the RB coefficients are approximated by separate NNs.

To demonstrate that the developed POD-NN approach may be used across a range of domain mappings, we compare different deformation scalings in Figure 6 (left), and unsurprisingly, larger deformations are harder to approximate. Not only is the mean field a worse predictor ($L = 0$), both the Galerkin-POD RB method and the POD-NN struggle to decrease the error below $8e-3$ for the largest deformation: while the error for $\theta = 0.1$ drops below $1e-4$, the error for $\theta = 0.5$ only drops below $1e-3$ for 30 modes, which is only a marginal improvement compared to the error of using only the mean field. That being said, these results were computed for a parameter dimension of size 50, which is a very challenging learning problem. This effect becomes clearly visible in Figure 6 (right), where we observe a significantly larger drop in error for parameter dimension size $J = 10$. Interestingly, in all cases, we observe a barrier in error for the POD-NN, while the error of the Galerkin-POD may increase intermediately but ultimately keeps decreasing in this case.

In Figure 7, we compare the effect of the different decays. For the algebraic decay, we seem to be unable to learn meaningful information past the first five modes. In this case the Galerkin-POD appears to perform much better, which may be attributed to overfitting in the training process as the parameter domain is sampled very sparsely. For the Matérn type decay, we observe a more clear decrease in error for both the POD-NN and the Galerkin-POD. Figure 8 shows the relative error in the RB coefficient. It is notable that the first seven coefficients have a lower error of around 10%, while the error can increase to up to 50% for the following coefficients. This is consistent with the barrier in error decay that we have observed: The neural network does not seem to learn useful information past the first eight modes.

Figure 9 explores the effect of different wave numbers κ . Perhaps unsurprisingly, higher frequencies are harder to approximate. For $\kappa = 16$, the mean field incurs an error of $5e-2$, which might be considered a large error for some applications, while the POD-NN and RB method lead to more reliable predictions with an error of $3e-3$, i.e. we again gain about a factor 10 in accuracy. Lastly, while the POD-NN method has similar or sometimes higher errors than the classic RB method, Figure 10 shows that the POD-NN is about a factor of 10000 faster. While the POD-NN method only requires an NN evaluation and some vector operations, the RB method requires full assembly of the linear system operators, which leads to this large

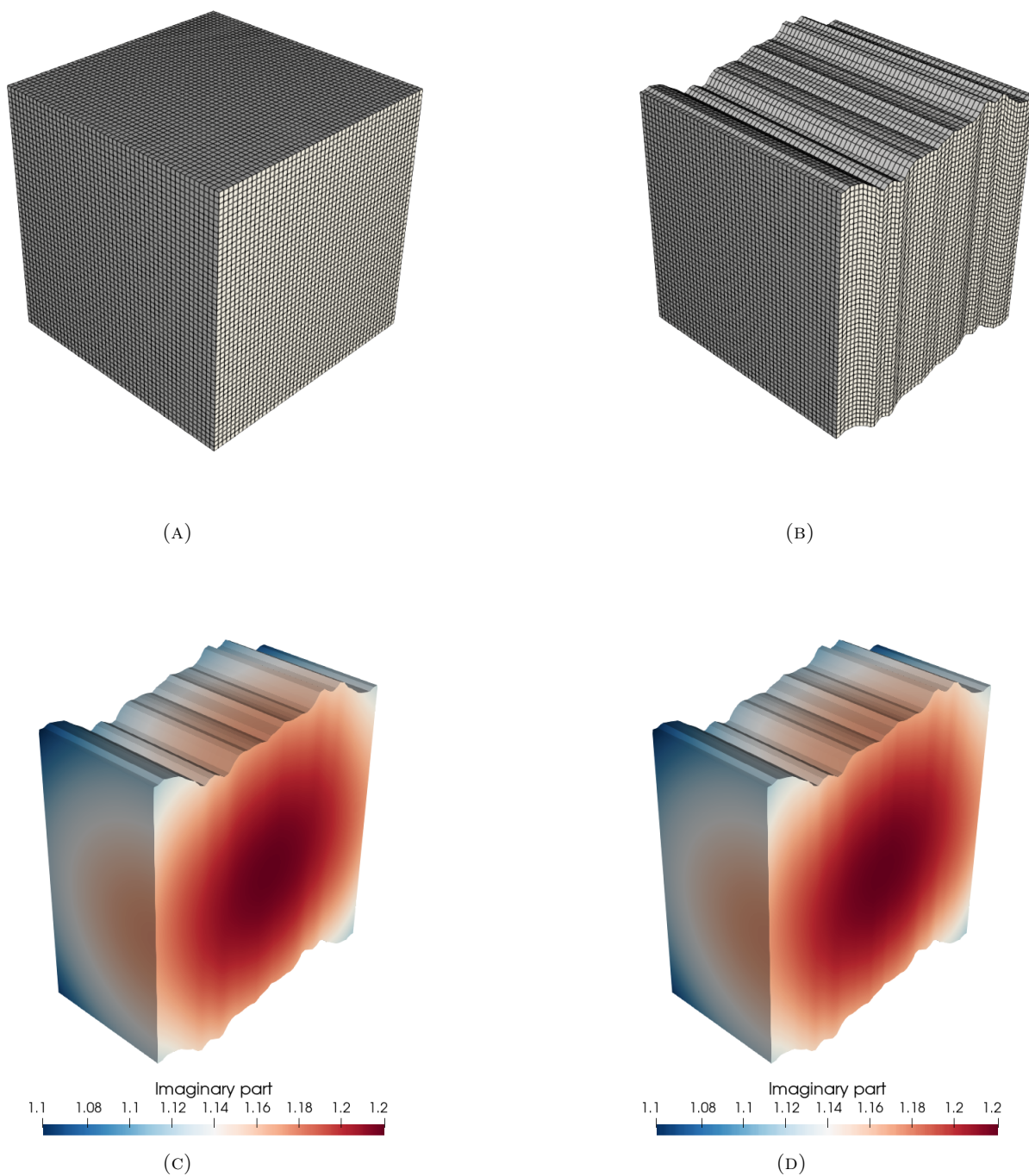


FIGURE 2. Computational meshes and graphical results for the Helmholtz problem: (A) reference mesh, on which the solutions are computed. (B) Physical domain. (C) Imaginary part of the full-order solution. (D) Imaginary part of the POD-NN prediction. The solution to the Helmholtz problem was computed for the parameters $\theta = 0.5$, $l = 0.1$, $\nu = 0.5$, and $J = 50$. The domain deformation is amplified by a factor of two for better visibility.

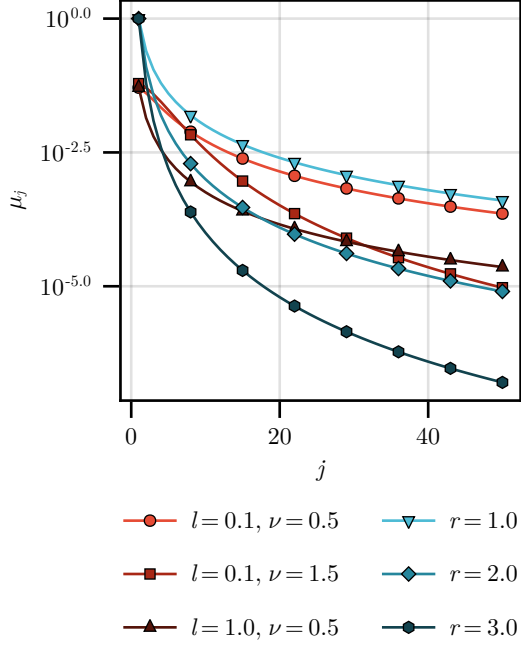


FIGURE 3. The first 50 coefficients μ_j for different parameters of algebraic (blue tones) and Matérn (red tones) decay.

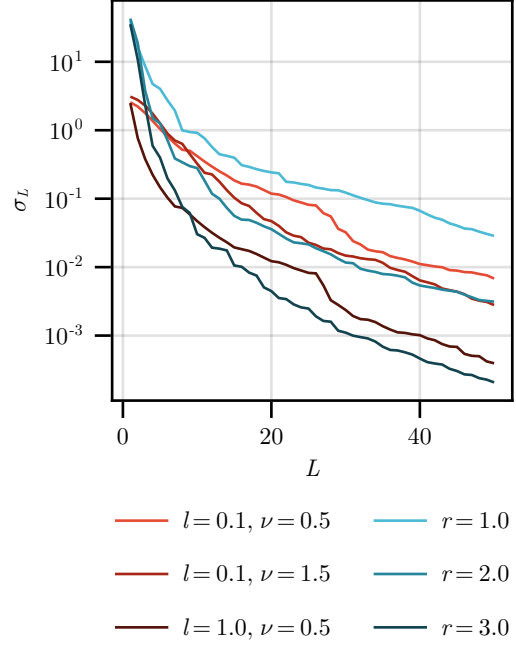


FIGURE 4. The singular values of 1024 snapshots for different parameters of algebraic (blue tones) and Matérn (red tones) decay. The input parameters originate from the same Halton sequence.

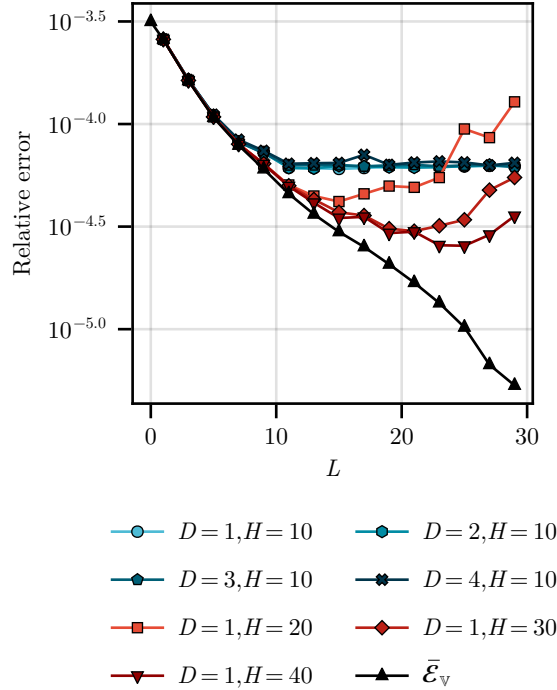


FIGURE 5. Test errors for different neural network architectures, i.e., different numbers of hidden layers D and neurons per layer H . All models were trained using Adam with learning rate $5e-4$, $\beta_1 = 0.8$ and $\beta_2 = 0.9$ for 4000 epochs. The networks were trained on 1024 snapshots sampled from a Halton sequence of Matérn decay parameters with the following settings: $\theta = 0.1$, $J = 50$, $\nu = 0.5$, $l = 0.1$.

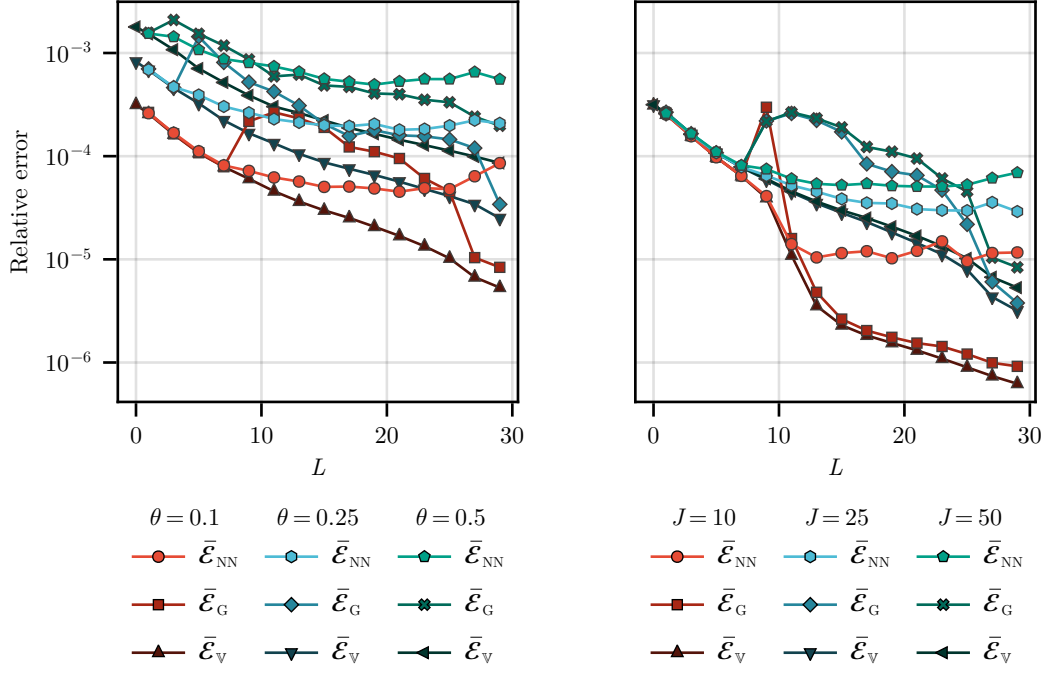


FIGURE 6. Test errors for deformation scalings (l.) and parameter dimensions (r.). All models were trained using Adam with learning rate $5e-4$, $\beta_1 = 0.8$ and $\beta_2 = 0.9$ for 4000 epochs. The networks were trained on 1024 snapshots sampled from a Halton sequence of Matérn decay parameters with the following settings: $\nu = 0.5, l = 0.1$.

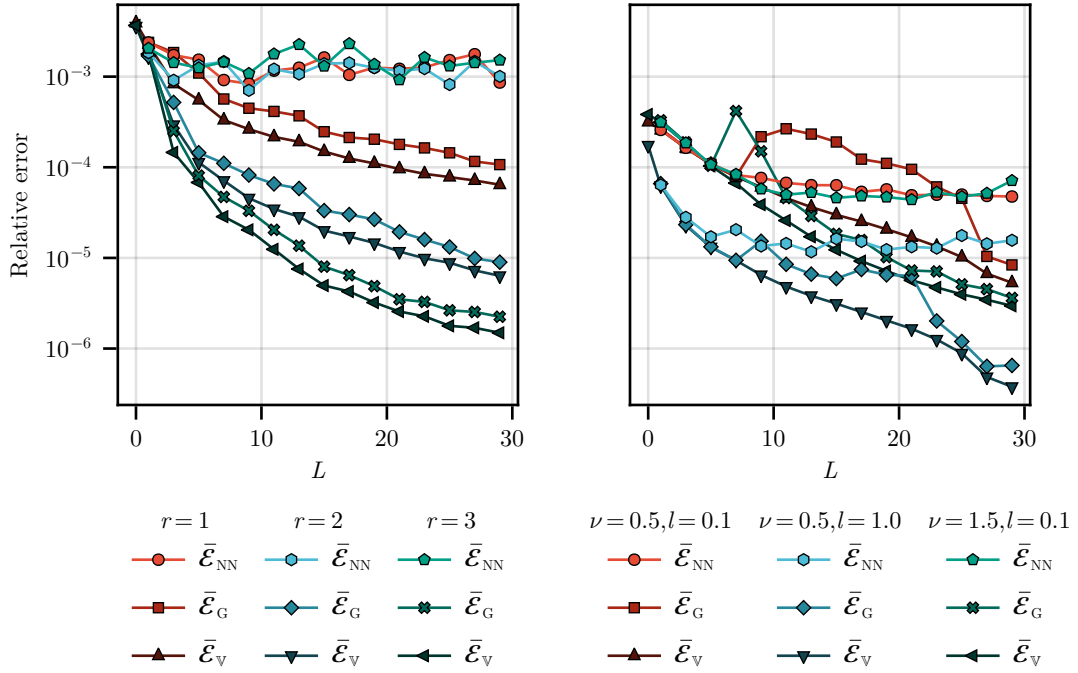


FIGURE 7. Test errors for algebraic decay (l.) and Matérn decay parameters (r.). All models were trained using Adam with learning rate $5e-4$, $\beta_1 = 0.8$ and $\beta_2 = 0.9$ for 4000 epochs. The networks were trained on 1024 snapshots sampled from a Halton sequence of corresponding decay type parameters with the following settings: $\theta = 0.1, J = 50$.

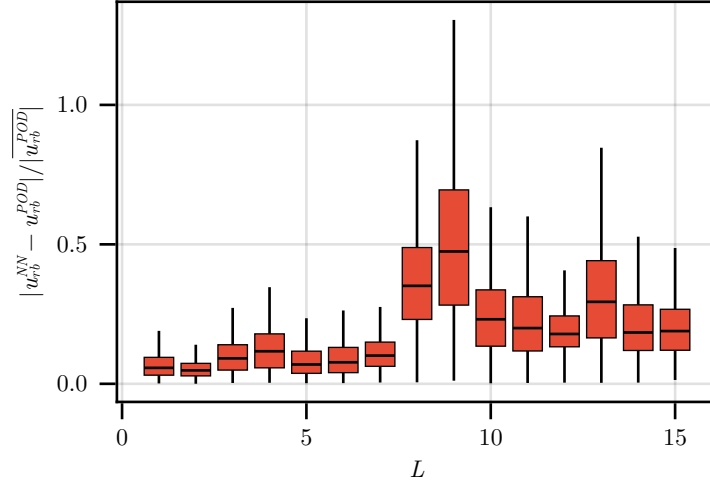


FIGURE 8. Errors relative to the mean reduced coefficient mode by mode committed by the neural network interpolation. The NN has $D = 2$ hidden layers and $H = 30$ neurons per layer and has been trained with the usual settings on 1024 snapshots (Halton sampling) of Matérn perturbations ($\nu = 0.5$, $l = 0.1$).

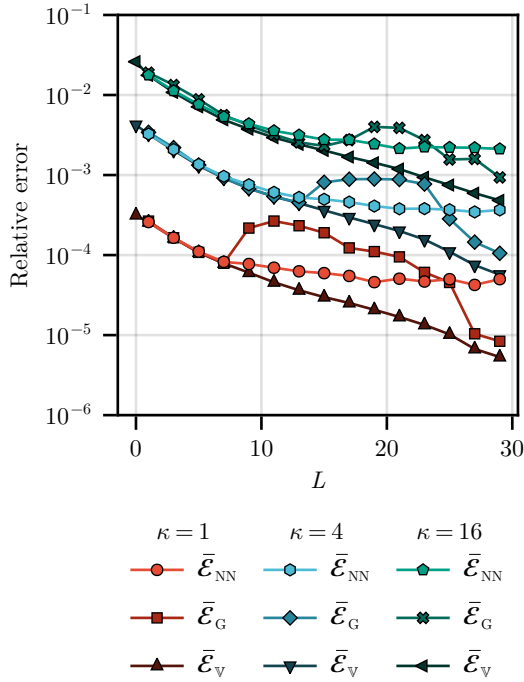


FIGURE 9. Test errors for different wavenumbers κ . All models were trained using Adam with learning rate $5e-4$, $\beta_1 = 0.8$ and $\beta_2 = 0.9$ for 4000 epochs. The networks were trained on 1024 snapshots sampled from a Halton sequence of Matérn decay parameters with the following settings: $\theta = 0.1$, $J = 50$, $\nu = 0.5$, $l = 0.1$.

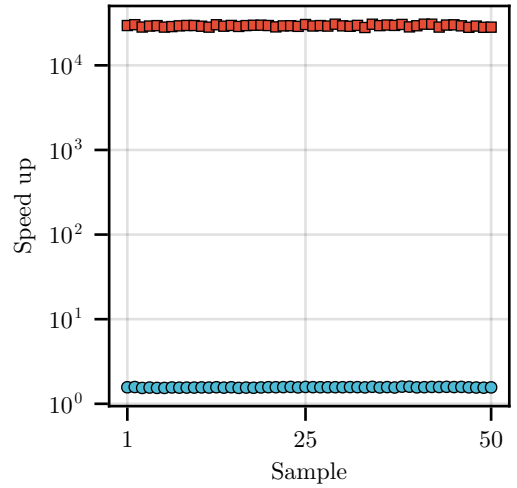


FIGURE 10. Speed up relative to the high-fidelity solver achieved with Intel(R) Xeon(R) Gold 6148 CPUs for the Galerkin-POD and POD-NN method, respectively.

discrepancy. In cases, where the mean field alone is not a reliable predictor, the proposed POD-NN method can thus be a valuable and efficient tool to approximate the parameter-to-solution map.

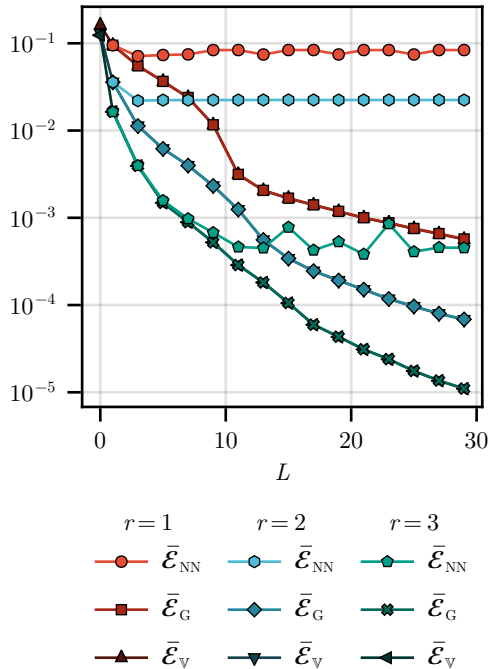


FIGURE 11. Test error for the Maxwell problem with different algebraic decay rates.

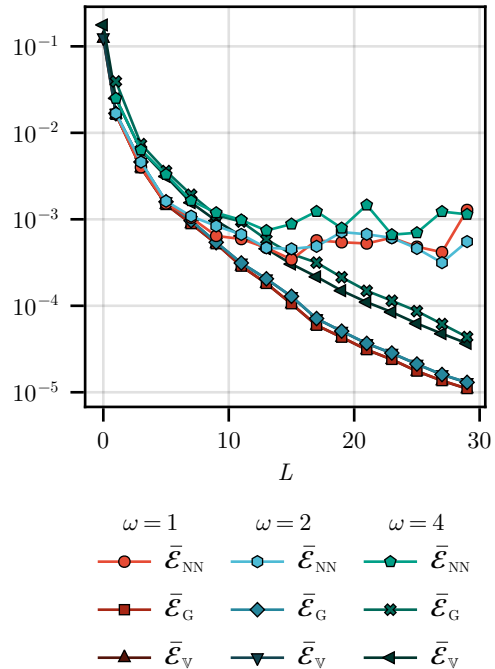


FIGURE 12. Test error for the Maxwell problem with different frequencies ω and algebraic coefficient decay with rate $r=3$.

Our experiments further indicate, that there is usually an “optimal” number of basis functions, for which the POD-NN achieves the lowest error or does not benefit from adding more RB modes. To achieve maximum efficiency in the online phase, it may thus be desirable to truncate to a certain number of basis functions. Alternatively, adding more training data, i.e. evaluate more HF snapshots, might be necessary to train the POD-NN optimally for a higher number of basis functions: it seems that fewer snapshots are required to find a good basis than for training the NN to learn the parameter to solution map.

5.4. Numerical Results for the Maxwell cavity problem. For this problem, we follow the problem setup described in Section 2.5 with the model constants set as $\omega = 1$, $\Lambda = 1 - \nu$, $\mu = 1$. The FE model uses first-order Nédélec elements with a resolution of 50 cells per side. The boundary variation is parametrized with an algebraic decay of dimension $J = 10$, with scaling $\theta = 0.1$. Once again, we generate a training set on a Halton sequence of 1024 points and a test set from Latin Hypercube sampling. In Figure 11, the error of the Galerkin-POD solution perfectly follows the projection error: it decreases monotonically when more basis functions are added, confirming the success of the RB construction. Figure 11 further shows that the mean field ($L=0$) is probably not a sufficient predictor in this case, as the error is larger than 10% for all algebraic decay rates. The Galerkin POD-NN also leads to satisfactory error for the strongest decay ($r=3$), which plateaus just below $1e-3$. For the slower decay rates, the error appears to plateau for $L > 2$, indicating that the NN is not able to learn the map from the parameters to the reduced coefficients for the additionally added basis functions. More data points in the parameter space are likely needed to achieve higher accuracy. In 12, we observe that the POD-NN method is also successful for higher circular frequencies of the Maxwell problem and provides vastly better accuracy than the mean prediction alone.

6. CONCLUDING REMARKS

In this work, we present a Galerkin POD-NN method for surrogate modeling of three-dimensional acoustic and electromagnetic wave problems with parametric-affine shape deformations. Using readily available results for the Maxwell cavity problem and our analysis for the Helmholtz impedance problem, we demonstrate the analytic or holomorphic dependency of the problem's solution upon such parametric shape deformations. Based on this analysis, we argue that computational models for this class of problems are amenable to complexity reduction using a projection-based reduced basis scheme irrespective of the dimensionality of the parametric domain. Following the same argument, the map from the parameters to the coefficients of the RB basis representation is also amenable to approximation, done here by using NNs. Unlike many commonly computational models for which the Galerkin POD-NN has been applied, the involved quantities are complex-valued. We propose a formulation in which we separate the reduced coefficients into their real and imaginary parts. In the training stage, we consider each as a separate trainable, real-valued output, thus allowing us to retain an NN with real-valued features.

Our numerical experiments indicate that the mean field may be a predictor of reasonable accuracy in some cases, whereas the POD-NN method can improve this by an order of magnitude or more. The success of the surrogate model also critically depends on the hyper-parameter choices of the original problem and interestingly seems to work well on the Matérn-type decay. We have further observed that for a given data set, there seems to be an optimal number of basis functions in terms of efficiency, as no more gains in accuracy can be achieved by increasing the basis size. While our theoretical investigations prove convergence rates of the reduced order approximation independent of the parameter dimension, the cost of accurately creating such a reduced order approximation still scales with the parametric dimension, e.g., via the low-discrepancy series or the number of training points that are required for the NN approximation. In principle, this may be addressed by using tailored, high-dimensional quadrature rules as in [39].

In the current work, the considerable computational cost of obtaining high fidelity training data for complex 3D problems, limited the size of our training data set, which also shows in the limited success for the most complex problems. In future work, it would be interesting to investigate whether adding more training data through a larger snapshot set or via an active learning scheme can overcome the error barriers that we observe. Similarly, including physical knowledge into the NN model, for instance, by adding the residual of the underlying PDE to the loss function, could improve performance when the training data set is of limited size. In addition, the method's performance could be improved by considering a multi-fidelity setup, where cheaply available lower-fidelity training data with e.g., reduced resolution, provides better coverage of the solution manifold.

APPENDIX A. PARAMETRIC HOLOMORPHY OF THE HELMHOLTZ PROBLEM

In [35], based on a small wavenumber assumption, it is proved parametric holomorphy of the parameter-to-solution map of the Helmholtz transmission problem. Here, we provide a complete argument for the Helmholtz impedance problem without the aforementioned assumption.

Proof of item (ii) in Proposition 3.2. As it has been proved before, the map $U \ni \mathbf{y} \mapsto \mathbf{T}(\mathbf{y}) \in W^{1,\infty}(D_0; \mathbb{R}^{3 \times 3})$ is $(\mathbf{b}, p, \varepsilon)$ -holomorphic for some $\varepsilon > 0$, see e.g. [14]. In turn this implies that the maps

$$U \ni \mathbf{y} \mapsto (d\mathbf{T}(\mathbf{y}))^{-\top} \in L^\infty(D_0; \mathbb{R}^{3 \times 3}) \quad \text{and} \quad U \ni \mathbf{y} \mapsto J(\mathbf{y}) \in L^\infty(D_0) \quad (\text{A.1})$$

are $(\mathbf{b}, p, \varepsilon)$ -holomorphic as well, which follows using [14]. In addition, according [18, Lemma 2.14] the map

$$U \ni \mathbf{y} \mapsto \hat{\nu}(\mathbf{y}) \in L^\infty(D_0; \mathbb{R}^3) \quad (\text{A.2})$$

is $(\mathbf{b}, p, \varepsilon)$ -holomorphic for some $\varepsilon > 0$, and as a consequence the map

$$U \ni \mathbf{y} \mapsto J_S(\mathbf{y}) \in L^\infty(D_0) \quad (\text{A.3})$$

is so as well with the same $\mathbf{b} \in \ell^p(\mathbb{N})$ and $p \in (0, 1)$, however possibly with a different $\varepsilon > 0$. In turn, these results imply that the map

$$\mathbb{U} \ni \mathbf{y} \mapsto \hat{\mathbf{a}}(\cdot, \cdot; \mathbf{y}) \in \mathcal{L}(H^1(\mathbb{D}_0) \times H^1(\mathbb{D}_0); \mathbb{C})$$

is $(\mathbf{b}, p, \varepsilon)$ -holomorphic for some $\varepsilon > 0$ and the same $\mathbf{b} \in \ell^p$ and $p \in (0, 1)$, where, for a Banach space X , $\mathcal{L}(X \times X; \mathbb{C})$ denotes the space of continuous sesquilinear forms in X , which equipped with the norm

$$\|\mathbf{b}\|_{\mathcal{L}(X \times X; \mathbb{C})} := \sup_{u, v \in X \setminus \{0\}} \frac{|\mathbf{b}(u, v)|}{\|u\|_X \|v\|_X}, \quad \mathbf{b} \in \mathcal{L}(X \times X; \mathbb{C}),$$

is a Banach space itself. Furthermore, the one can also verify based on the previously stated results that the map

$$\mathbb{U} \ni \mathbf{y} \mapsto \hat{\ell}(\cdot, \mathbf{y}) \in (H^1(\mathbb{D}_0))'$$

is $(\mathbf{b}, p, \varepsilon)$ -holomorphic. In addition, for each $\mathbf{y} \in \mathbb{U}$ the sesquilinear form satisfies a Garding's inequality, with in turn implies for each $\mathbf{y} \in \mathbb{U}$ inf-sup conditions of the form

$$\begin{aligned} \inf_{\hat{v} \in H^1(\mathbb{D}_0) \setminus \{0\}} \sup_{\hat{w} \in H^1(\mathbb{D}_0) \setminus \{0\}} \frac{|\hat{\mathbf{a}}(\hat{v}, \hat{w}; \mathbf{y})|}{\|\hat{u}\|_X \|\hat{v}\|_X} &\geq \alpha, \quad \text{and} \\ \inf_{\hat{w} \in H^1(\mathbb{D}_0) \setminus \{0\}} \sup_{\hat{v} \in H^1(\mathbb{D}_0) \setminus \{0\}} \frac{|\hat{\mathbf{a}}(\hat{v}, \hat{w}; \mathbf{y})|}{\|\hat{u}\|_X \|\hat{v}\|_X} &> \alpha \end{aligned}$$

for a constant $\alpha > 0$ independent of $\mathbf{y} \in \mathbb{U}$. By using a perturbation argument we may conclude that there exists $\tilde{\alpha}(\tilde{\varepsilon}) > 0$ depending on some $\tilde{\varepsilon} > 0$ such that for any $(\mathbf{b}, \tilde{\varepsilon})$ -admissible (as in Definition 3.1), for each $\mathbf{z} \in \mathcal{O}_\rho$ we have inf-sup conditions of the form

$$\begin{aligned} \inf_{\hat{v} \in H^1(\mathbb{D}_0) \setminus \{0\}} \sup_{\hat{w} \in H^1(\mathbb{D}_0) \setminus \{0\}} \frac{|\hat{\mathbf{a}}(\hat{v}, \hat{w}; \mathbf{z})|}{\|\hat{u}\|_X \|\hat{v}\|_X} &\geq \tilde{\alpha}(\tilde{\varepsilon}), \quad \text{and} \\ \inf_{\hat{w} \in H^1(\mathbb{D}_0) \setminus \{0\}} \sup_{\hat{v} \in H^1(\mathbb{D}_0) \setminus \{0\}} \frac{|\hat{\mathbf{a}}(\hat{v}, \hat{w}; \mathbf{z})|}{\|\hat{u}\|_X \|\hat{v}\|_X} &> \tilde{\alpha}(\tilde{\varepsilon}), \end{aligned}$$

where for each $\mathbf{z} \in \mathcal{O}_\rho$ by $\hat{\mathbf{a}}(\cdot, \cdot; \mathbf{z})$ we refer to the extension of $\hat{\mathbf{a}}(\cdot, \cdot; \mathbf{y})$ to complex-valued parametric input. The existence of this extension is guaranteed by the existence of equivalent extension for the maps defined in (A.1), (A.2), and (A.3). Hence, recalling [12, Theorem 4.1] we may conclude that the map

$$\mathbb{U} \ni \mathbf{y} \mapsto \hat{u}(\mathbf{y}) \in H^1(\mathbb{D}_0)$$

is $(\mathbf{b}, p, \varepsilon)$ -holomorphic with the same $\mathbf{b} \in \ell^p(\mathbb{N})$ and $p \in (0, 1)$ and for some $\varepsilon > 0$, where, for each $\mathbf{y} \in \mathbb{U}$, $\hat{u}(\mathbf{y})$ is the solution to Problem 2.4. A similar argument holds true when we consider the discrete parameter-to-solution map. However, at it is customary for problems satisfying a Garding-type inequality, there exists a $h_0 > 0$ such that for any $h < h_0$ the map

$$\mathbb{U} \ni \mathbf{y} \mapsto \hat{u}_h(\mathbf{y}) \in V_h$$

is $(\mathbf{b}, p, \varepsilon)$ -holomorphic for some $\varepsilon > 0$ independent of the discretization $h > 0$. □

APPENDIX B. ADDITIONAL FIGURES

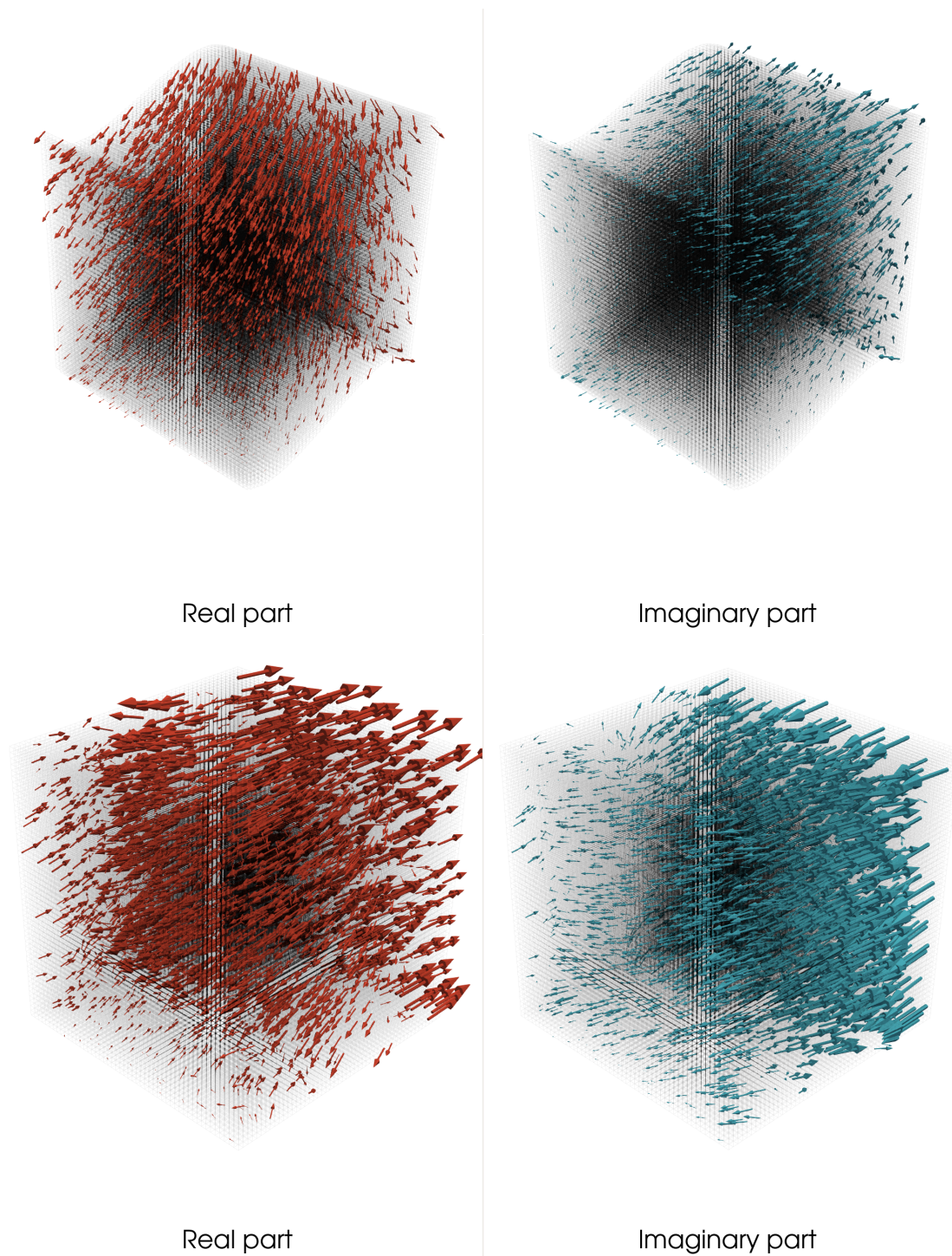


FIGURE 13. Glyph plot of the solution field (A) and the first POD mode (B) of the Maxwell problem with algebraic decay ($r = 1.0$). The length of the glyphs is given by the real- and imaginary parts, respectively, where the values have been rescaled to 20% in (B) for better visibility.

REFERENCES

- [1] B. ADCOCK, S. BRUGIAPAGLIA, N. DEXTER, AND S. MORAGA, *Near-optimal learning of Banach-valued, high-dimensional functions via deep neural networks*, arXiv preprint arXiv:2211.12633, (2022).
- [2] R. AYLWIN, C. JEREZ-HANCKES, C. SCHWAB, AND J. ZECH, *Domain uncertainty quantification in computational electromagnetics*, SIAM/ASA Journal on Uncertainty Quantification, 8 (2020), pp. 301–341.
- [3] S. BADIA AND F. VERDUGO, *Gridap: An extensible finite element toolbox in Julia*, Journal of Open Source Software, 5 (2020), p. 2520.
- [4] K. BHATTARAI, S. SILVA, K. SONG, A. URBAS, S. J. LEE, Z. KU, AND J. ZHOU, *Metamaterial perfect absorber analyzed by a meta-cavity model consisting of multilayer metasurfaces*, Scientific Reports, 7 (2017).
- [5] D. BOFFI, F. BREZZI, AND M. FORTIN, *Mixed Finite Element Methods and Applications*, Springer Berlin Heidelberg, 2013.
- [6] T. BORRVALL AND J. PETERSSON, *Topology optimization of fluids in stokes flow*, International journal for numerical methods in fluids, 41 (2003), pp. 77–107.
- [7] R. E. CAFLISCH, *Monte Carlo and quasi-monte Carlo methods*, Acta numerica, 7 (1998), pp. 1–49.
- [8] J. E. CASTRILLÓN-CANDÁS, F. NOBILE, AND R. F. TEMPONE, *Analytic regularity and collocation approximation for elliptic PDEs with random domain deformations*, Computers & Mathematics with Applications, 71 (2016), pp. 1173–1197.
- [9] P. CHEN AND C. SCHWAB, *Model order reduction methods in computational uncertainty quantification*, in Handbook of Uncertainty Quantification, Springer International Publishing, 2015, pp. 1–53.
- [10] W. CHEN, Q. WANG, J. S. HESTHAVEN, AND C. ZHANG, *Physics-informed machine learning for reduced-order modeling of nonlinear problems*, Journal of Computational Physics, 446 (2021), p. 110666.
- [11] Y.-B. CHEN AND Z. ZHANG, *Design of tungsten complex gratings for thermophotovoltaic radiators*, Optics Communications, 269 (2007), pp. 411–417.
- [12] A. CHKIFA, A. COHEN, AND C. SCHWAB, *Breaking the curse of dimensionality in sparse polynomial approximation of parametric PDEs*, Journal de Mathématiques Pures et Appliquées, 103 (2015), pp. 400–428.
- [13] A. COHEN AND R. DEVORE, *Kolmogorov widths under holomorphic mappings*, IMA Journal of Numerical Analysis, 36 (2016), pp. 1–12.
- [14] A. COHEN, C. SCHWAB, AND J. ZECH, *Shape Holomorphy of the stationary Navier–Stokes equations*, SIAM Journal on Mathematical Analysis, 50 (2018), pp. 1720–1752.
- [15] M. DALLA RIVA, P. LUZZINI, AND P. MUSOLINO, *Shape analyticity and singular perturbations for layer potential operators*, ESAIM: Mathematical Modelling and Numerical Analysis, 56 (2022), pp. 1889–1910.
- [16] J. DICK, F. Y. KUO, Q. T. LE GIA, D. NUYENS, AND C. SCHWAB, *Higher order QMC Petrov–Galerkin discretization for affine parametric operator equations with random field inputs*, SIAM Journal on Numerical Analysis, 52 (2014), pp. 2676–2702.
- [17] J. DICK, Q. T. LE GIA, AND C. SCHWAB, *Higher-order Quasi-Monte Carlo integration for holomorphic, parametric operator equations*, SIAM/ASA Journal on Uncertainty Quantification, 4 (2016), pp. 48–79.
- [18] J. DÖLZ AND F. HENRÍQUEZ, *Parametric shape holomorphy of boundary integral operators with applications*, arXiv preprint arXiv:2305.19853, (2023).
- [19] A. ERN AND J.-L. GUERMOND, *Finite element quasi-interpolation and best approximation*, ESAIM: Mathematical Modelling and Numerical Analysis, 51 (2017), pp. 1367–1385.
- [20] ———, *Finite Elements I*, Springer International Publishing, 2021.
- [21] ———, *Finite Elements II*, Springer International Publishing, 2021.
- [22] M. GANESH, F. Y. KUO, AND I. H. SLOAN, *Quasi-Monte Carlo finite element analysis for wave propagation in heterogeneous random media*, SIAM/ASA Journal on Uncertainty Quantification, 9 (2021), pp. 106–134.
- [23] M. GUO AND J. S. HESTHAVEN, *Reduced order modeling for nonlinear structural analysis using gaussian process regression*, Computer methods in applied mechanics and engineering, 341 (2018), pp. 807–826.
- [24] A.-L. HAJI-ALI, H. HARBRECHT, M. PETERS, AND M. SIEBENMORGEN, *Novel results for the anisotropic sparse grid quadrature*, Journal of Complexity, 47 (2018), pp. 62–85.
- [25] J. H. HALTON, *On the efficiency of certain quasi-random sequences of points in evaluating multi-dimensional integrals*, Numerische Mathematik, 2 (1960), pp. 84–90.
- [26] H. HARBRECHT, M. PETERS, AND M. SIEBENMORGEN, *Analysis of the domain mapping method for elliptic diffusion problems on random domains*, Numerische Mathematik, 134 (2016), pp. 823–856.
- [27] H. HARBRECHT AND M. SCHMIDLIN, *Multilevel quadrature for elliptic problems on random domains by the coupling of FEM and BEM*, Stochastics and Partial Differential Equations: Analysis and Computations, 10 (2022), pp. 1619–1650.
- [28] F. HENRÍQUEZ, *Shape Uncertainty Quantification in Acoustic Scattering*, PhD thesis, ETH Zurich, 2021.
- [29] F. HENRÍQUEZ AND J. PINTO, *Reduced basis method for the elastic scattering by multiple shape-parametric open arcs in two dimensions*, arXiv preprint arXiv:2403.10933, (2024).
- [30] F. HENRÍQUEZ AND C. SCHWAB, *Shape holomorphy of the Calderón projector for the Laplacian in \mathbb{R}^2* , Integral Equations and Operator Theory, 93 (2021), p. 43.
- [31] L. HERRMANN, J. A. OPSCHOOR, AND C. SCHWAB, *Constructive deep ReLU neural network approximation*, Journal of Scientific Computing, 90 (2022), pp. 1–37.

- [32] L. HERRMANN, C. SCHWAB, AND J. ZECH, *Deep neural network expression of posterior expectations in Bayesian PDE inversion*, Inverse Problems, 36 (2020), p. 125011.
- [33] J. HESTHAVEN AND S. UBBIALI, *Non-intrusive reduced order modeling of nonlinear problems using neural networks*, Journal of Computational Physics, 363 (2018), pp. 55–78.
- [34] J. S. HESTHAVEN, G. ROZZA, B. STAMM, ET AL., *Certified reduced basis methods for parametrized partial differential equations*, vol. 590, Springer, 2016.
- [35] R. HIPTMAIR, L. SCARABOSIO, C. SCHILLINGS, AND C. SCHWAB, *Large deformation shape uncertainty quantification in acoustic scattering*, Advances in Computational Mathematics, 44 (2018), pp. 1475–1518.
- [36] M. INNES, *Flux: Elegant machine learning with julia*, Journal of Open Source Software, 3 (2018), p. 602.
- [37] C. JEREZ-HANCKES, C. SCHWAB, AND J. ZECH, *Electromagnetic wave scattering by random surfaces: Shape holomorphy*, Mathematical Models and Methods in Applied Sciences, 27 (2016), pp. 2229–2259.
- [38] S. LANTHALER, *Operator learning with pca-net: upper and lower complexity bounds*, arXiv preprint arXiv:2303.16317, (2023).
- [39] M. LONGO, S. MISHRA, T. K. RUSCH, AND C. SCHWAB, *Higher-order quasi-monte carlo training of deep neural networks*, SIAM Journal on Scientific Computing, 43 (2021), pp. A3938–A3966.
- [40] K. O. LYE, S. MISHRA, AND D. RAY, *Deep learning observables in computational fluid dynamics*, Journal of Computational Physics, 410 (2020), p. 109339.
- [41] S. MISHRA AND T. K. RUSCH, *Enhancing accuracy of deep learning algorithms by training with low-discrepancy sequences*, SIAM Journal on Numerical Analysis, 59 (2021), pp. 1811–1834.
- [42] P. MONK, *Finite Element Methods for Maxwell's Equations*, OXFORD UNIV PR, June 2003.
- [43] F. NOBILE, R. TEMPONE, AND C. G. WEBSTER, *An anisotropic sparse grid stochastic collocation method for partial differential equations with random input data*, SIAM Journal on Numerical Analysis, 46 (2008), pp. 2411–2442.
- [44] J. A. OPSCHOOR, C. SCHWAB, AND J. ZECH, *Exponential ReLU DNN expression of holomorphic maps in high dimension*, Constructive Approximation, 55 (2022), pp. 537–582.
- [45] A. B. OWEN, *Monte carlo variance of scrambled net quadrature*, SIAM Journal on Numerical Analysis, 34 (1997), pp. 1884–1910.
- [46] J. PINTO, F. HENRÍQUEZ, AND C. JEREZ-HANCKES, *Shape holomorphy of boundary integral operators on multiple open arcs*, Journal of Fourier Analysis and Applications, 30 (2024), p. 14.
- [47] C. PRUD'HOMME, D. V. ROVAS, K. VEROY, L. MACHIELS, Y. MADAY, A. T. PATERA, AND G. TURINICI, *Reliable real-time solution of parametrized partial differential equations: Reduced-basis output bound methods*, J. Fluids Eng., 124 (2002), pp. 70–80.
- [48] A. QUARTERONI, A. MANZONI, AND F. NEGRI, *Reduced Basis Methods for Partial Differential Equations*, Springer International Publishing, 2016.
- [49] G. ROZZA, *Fundamentals of reduced basis method for problems governed by parametrized pdes and applications*, in Separated Representations and PGD-Based Model Reduction: Fundamentals and Applications, Springer, 2014, pp. 153–227.
- [50] C. SCHWAB AND J. ZECH, *Deep learning in high dimension: Neural network expression rates for generalized polynomial chaos expansions in UQ*, Analysis and Applications, 17 (2019), pp. 19–55.
- [51] R. C. SMITH, *Uncertainty quantification: theory, implementation, and applications*, vol. 12, Siam, 2013.
- [52] I. M. SOBOL', *On the distribution of points in a cube and the approximate evaluation of integrals*, Zhurnal Vychislitel'noi Matematiki i Matematicheskoi Fiziki, 7 (1967), pp. 784–802.
- [53] E. A. SPENCE AND J. WUNSCH, *Wavenumber-explicit parametric holomorphy of helmholtz solutions in the context of uncertainty quantification*, SIAM/ASA Journal on Uncertainty Quantification, 11 (2023), pp. 567–590.
- [54] F. TRÖLTZSCH, *Optimal control of partial differential equations: theory, methods, and applications*, vol. 112, American Mathematical Soc., 2010.
- [55] A. VAN DEN BOS, *Parameter estimation for scientists and engineers*, John Wiley & Sons, 2007.
- [56] C. K. WILLIAMS AND C. E. RASMUSSEN, *Gaussian processes for machine learning*, vol. 2, MIT press Cambridge, MA, 2006.
- [57] J. ZECH AND C. SCHWAB, *Convergence rates of high dimensional Smolyak quadrature*, ESAIM: Mathematical Modelling and Numerical Analysis, 54 (2020), pp. 1259–1307.